Zooming in on accretion - I. The structure of halo gas

Dylan Nelson[1]⋆, Shy Genel[1,2]†, Annalisa Pillepich[1], Mark Vogelsberger[3],
Volker Springel[4,5], Lars Hernquist[1]

[1] *Harvard-Smithsonian Center for Astrophysics, 60 Garden Street, Cambridge, MA, 02138, USA*
[2] *Department of Astronomy, Columbia University, 550 West 120th Street, New York, NY, 10027, USA*
[3] *Kavli Institute for Astrophysics and Space Research, Department of Physics, MIT, Cambridge, MA, 02139, USA*
[4] *Heidelberg Institute for Theoretical Studies, Schloss-Wolfsbrunnenweg 35, 69118 Heidelberg, Germany*
[5] *Zentrum für Astronomie der Universität Heidelberg, ARI, Mönchhofstr. 12-14, 69120 Heidelberg, Germany*

9 March 2015

ABSTRACT

We study the properties of gas in and around $10^{12} \, \mathrm{M}_\odot$ haloes at $z = 2$ using a suite of high-resolution cosmological hydrodynamic 'zoom' simulations. We quantify the thermal and dynamical structure of these gaseous reservoirs in terms of their mean radial distributions and angular variability along different sightlines. With each halo simulated at three levels of increasing resolution, the highest reaching a baryon mass resolution of ∼10,000 solar masses, we study the interaction of filamentary inflow and the quasi-static hot halo atmosphere. We highlight the discrepancy between the spatial resolution available in the halo gas as opposed to within the galaxy itself, and find that stream morphologies become increasingly complex at higher resolution, with large coherent flows revealing density and temperature structure at progressively smaller scales. Moreover, multiple gas components co-exist at the same radius within the halo, making radially averaged analyses misleading. This is particularly true where the hot, quasi-static, high entropy halo atmosphere interacts with cold, rapidly inflowing, low entropy accretion. We investigate the process of gas virialization and identify different regimes for the heating of gas as it accretes from the intergalactic medium. Haloes at this mass have a well-defined virial shock, associated with a sharp jump in temperature and entropy at $\gtrsim 1.25 \, r_{\rm vir}$. The presence, radius, and radial width of this boundary feature, however, vary not only from halo to halo, but also as a function of angular direction, covering roughly ∼85% of the 4π sphere. Our findings are relevant for the proper interpretation of observations pertaining to the circumgalactic medium, including evidence for large amounts of cold gas surrounding massive haloes at intermediate redshifts.

Key words: methods: numerical – galaxies: evolution – galaxies: formation – galaxies: haloes – cosmology: theory

1 INTRODUCTION

Initially following the gravitational collapse of a dark matter overdensity, gaseous haloes subsequently grow through the accretion of baryons from the intergalactic medium (IGM). Their evolving structure across cosmic time has been the subject of theoretical as well as observational interest for several decades. As the transitional state between the diffuse IGM and the star-forming interstellar medium of galaxies, these gas reservoirs regulate the stellar growth of forming galaxies. Understanding not only the structure of halo gas, but also its origin and subsequent evolution, is therefore essential for any comprehensive theory of galaxy formation.

Although the accretion of gas will follow that of dark matter, the presence of additional physical processes including hydrodynamical forces and radiative cooling imply additional complexity for the acquisition of baryons. In the classic picture, gas accreting from the intergalactic medium will shock heat to the virial temperature of the halo. If the radiative cooling timescale is sufficiently long, it will then form a hot, pressure supported atmosphere in approximate equilibrium (Rees & Ostriker 1977; Silk 1977; White & Rees 1978). Cooling can proceed, delivering gas into the

halo centre (White & Frenk 1991). For sufficiently low mass haloes, this timescale will be short enough that a 'stable virial shock' cannot develop, and gas accretion from the IGM will proceed as rapidly as dynamically allowed (Birnboim & Dekel 2003a). However, this theoretical foundation is largely based on a one-dimensional picture, while dark matter haloes and their gaseous counterparts are decidedly not spherically symmetric. Numerical hydrodynamical simulations have indicated that galaxies can acquire their gas in a fundamentally different manner (Katz et al. 2003; Abadi et al. 2003; Kereš et al. 2005; Ocvirk et al. 2008). In particular, finding that coherent, filamentary inflows can fuel star formation in a central galaxy while avoiding shock heating to the virial temperature. Such streams arise naturally from the topology of large-scale structure, particularly at high redshifts of $z \gtrsim 2$ (Dekel et al. 2009; Agertz et al. 2009; Kereš et al. 2009; Danovich et al. 2012).

Gas inflow has been studied in the context of many key questions in galaxy formation, most fundamental of which is perhaps its link to star formation (Oppenheimer et al. 2010; Gabor & Bournaud 2014; Sánchez Almeida et al. 2014) and the process of quenching (Birnboim & Dekel 2003b; Birnboim et al. 2007; Gabor & Davé 2012; Feldmann & Mayer 2015; Aragon-Calvo et al. 2014). The accretion of cosmological gas will leave a fundamental imprint on the thermal and dynamical properties of the quasi-static halo gas, as will outflows from energetic feedback processes in galaxies (Putman et al. 2012). By studying the properties of this halo gas we can investigate the interplay of inflows and outflows with metals (e.g. Shen et al. 2013; Hummels et al. 2013; Ford et al. 2014) as well as with neutral hydrogen (e.g. Faucher-Giguère et al. 2011; Faucher-Giguere et al. 2014; Fumagalli et al. 2014).

The state of gas in and around galaxy haloes has also received significant observational scrutiny in the local universe as well as at $z \sim 2$, near the peak of the cosmic star formation rate. At these high redshifts both hydrogen and metals are accessible as absorption signatures in sightlines towards background objects, enabling a probe of the interaction between galaxies and the IGM in the vicinity at this period of rapid stellar growth. Efforts include the 'quasars probing quasars' series (Hennawi et al. 2006; Prochaska et al. 2013, 2014), the Keck Baryonic Structure Survey (Steidel et al. 2010; Rudie et al. 2012, 2013; Turner et al. 2014b), and other $2 \lesssim z \lesssim 3$ studies (Simcoe et al. 2006; Pieri et al. 2014; Rubin et al. 2014; Crighton et al. 2015). Collectively they probe the covering fractions, radial profiles, and kinematics of HI and many metal ions including those of oxygen, carbon, neon, silicon, and magnesium.

Perhaps the most puzzling discovery which remains at the present unreconciled with theory is the presence of a large amount of cold ($\sim 10^4$ K), metal-enriched gas widely distributed at least out to the virial radius of massive ($10^{12} \sim 10^{12.5}$ M$_\odot$) haloes. For instance, Prochaska et al. (2014) find a covering fraction approaching unity for strong C II absorption at a hundred physical kiloparsecs or more from the halo centre. The origin of this gas and the process by which it is either maintained or replenished within the hot halo remains uncertain. Consequently, this regime provides a powerful test-bed for current hydrodynamic simulations of galaxy formation. Not only in terms of the physical modelling of feedback and the resultant galactic-scale outflows

(Muratov et al. 2015), but more fundamentally in terms of our ability to resolve the gas-dynamical processes and the spatial scales relevant for the physics of cosmological gas accretion.

This paper investigates the thermal and dynamical structure of halo gas in eight simulated $\simeq 10^{12}$ M$_\odot$ haloes at $z = 2$. In Section 2 we describe the simulation technique and analysis methodology. Section 3 addresses the issue of resolution for halo gas and presents a visual overview of the systems. Section 4 considers the radially averaged gas properties, while Section 5 expands this analysis to explore the angular variability of halo structure. We discuss our results in the context of observations of the gas content of haloes in Section 6 and summarize our conclusions in Section 7.

2 METHODS

2.1 Initial Conditions

All simulations evolve initial conditions which are a random realization of a WMAP-9 consistent cosmology ($\Omega_{\Lambda,0} = 0.736$, $\Omega_{m,0} = 0.264$, $\Omega_{b,0} = 0.0441$, $\sigma_8 = 0.805$, $n_s = 0.967$ and $h = 0.712$). We use the MUSIC code (Hahn & Abel 2011, v1.5, r375) to generate multi-mass 'zoom' ICs, under the 2LPT approximation and with a tabulated transfer function from CAMB (Lewis et al. 2000). First, we evolve a low resolution, dark matter only uniform periodic box of sidelength $20h^{-1}$ Mpc $\simeq 28.6$ Mpc with 128^3 particles ('L7', where L$N = 2^N$), from a starting redshift of $z = 99$ down to $z = 2$. At this redshift, there are 20 haloes with total mass between $10^{11.8}$M$_\odot$ and $10^{12.4}$M$_\odot$ from which we choose eight at random to re-simulate at higher resolution. We do not select for any additional properties – e.g., merger history or environment. All particles within some factor of the virial radius of each selected halo (ranging from $3.6\,r_{\rm vir}$ to $7.0\,r_{\rm vir}$ in all cases, see Oñorbe et al. (2014) for relevant considerations) are identified at $z = 2$. We take $r_{\rm vir} = r_{200,{\rm crit}}$ the radius enclosing a mean overdensity 200 times the critical density. This factor was chosen by trial and error with evaluation of contamination levels in low resolution test runs. The convex hull of the $z = 99$ positions of all selected particles is then used to define the high resolution refinement region.

For each halo, new initial conditions are generated for each of L9, L10, and L11, corresponding to 512^3, 1024^3, and 2048^3 total particles if the parent box were to be simulated at a uniform resolution. We note that the mass resolution of L11 is between Aquarius levels '3' and '4' (of e.g. Marinacci et al. 2014a; Scannapieco et al. 2012), while the resolution of L9 is approximately equal to the resolution in modern, large volume cosmological simulations. Baryons are included by splitting each dark matter particle according to the cosmological baryon fraction, into one DM particle and one gas cell, such that the centre of mass position and velocity are preserved. Therefore we do not consider a separate transfer function for the baryonic component. The files required to generate our initial conditions, including the CAMB transfer function, noise seeds, and convex hull point sets, are made

Table 1. General characteristics of our three resolution levels, L9, L10, and L11. First, the effective resolution of an equivalent uniform box. Next, the mean number of high resolution gas elements, number of timesteps, baryonic mass resolution, and dark matter mass resolution. The Plummer equivalent comoving gravitational softening lengths, and their physical values at $z=2$. The minimum gas cell spatial size in physical parsecs at $z=2$, and the mean gas cell spatial size in the halo, between $0.5\,r_{\rm vir}$ and $1.0\,r_{\rm vir}$, in physical kiloparsecs at $z=2$.

Res	$N_{\rm part}^{\rm eff}$	$N_{\rm part}^{\rm HR}$	Δt [#]	$m_{\rm baryon}$ [M$_\odot$]	$m_{\rm DM}$ [M$_\odot$]	$\epsilon_{\rm grav}^{\rm comoving}$ [pc]	$\epsilon_{\rm grav}^{z=2}$ [pc]	$r_{\rm cell}^{\rm min}$ [pc]	$r_{\rm cell}^{\rm halo}$ [kpc]
L9	512^3	800,000	80,000	1.0×10^6	5.1×10^6	1430	480	31	2.7
L10	1024^3	7,000,000	260,000	1.3×10^5	6.4×10^5	715	240	11	1.6
L11	2048^3	64,000,000	870,000	1.6×10^4	8.0×10^4	357	120	3.3	0.8

Table 2. Details on the eight simulated haloes: the total halo mass and (physical) virial radius at $z = 2$ from the parent box. The radius of the enclosing sphere at $z = 2$ used to define the Lagrangian region, in terms of $r_{\rm vir}$, and the number of high resolution elements, for each of dark matter and gas. Both are listed for the L11 level only. The minimum radius from the halo centre reached by (i) contaminating low resolution dark matter particles and (ii) Monte Carlo tracers originating in low resolution gas cells, in units of $r_{\rm vir}$. The total number of timesteps to reach $z=2$.

Halo #	$M_{\rm halo}^{\rm par}$ [log M$_\odot$]	$r_{\rm vir}^{\rm par}$ [kpc]	$r_{\rm HR}^{\rm L11}$ [$r_{\rm vir}$]	$N_{\rm HR}^{\rm L11}$ [10^6]	$r_{\rm LR}^{\rm min}$ [$r_{\rm vir}$]$_{\rm dm}$	$r_{\rm LR}^{\rm min}$ [$r_{\rm vir}$]$_{\rm tr}$	Δt #
h0	12.1	114	3.6	70.0	1.77	2.16	829714
h1	12.1	104	4.8	66.7	2.12	2.75	701681
h2	11.9	92	6.0	24.2	2.83	3.02	955189
h3	11.9	96	7.0	33.9	2.74	3.23	812983
h4	12.0	103	6.0	68.4	2.13	2.89	861224
h5	12.0	103	4.2	59.9	1.04	1.04	931088
h6	12.1	97	4.8	74.4	1.32	1.59	980918
h7	11.9	94	4.4	52.8	0.94	1.93	866242

publicly available online[1]. The fundamental characteristics of each resolution level are given in Table 1, while the physical properties and numerical details for each of the eight haloes are detailed in Table 2.

2.2 Simulation Code and Physics

We employ the AREPO code (Springel 2010, r25505) to solve the coupled equations of ideal continuum hydrodynamics and self-gravity. An unstructured, moving, Voronoi tessellation of the domain provides the spatial discretization for Godunov's method with a directionally un-split MUSCL-Hancock scheme (van Leer 1977) and an exact Riemann solver, obtaining second order accuracy in space. Since we allow the mesh generating sites to move, with a velocity equal to the local fluid velocity field modulated by corrections required to maintain the regularity of the mesh, this numerical approach would be classified as an Arbitrary Lagrangian-Eulerian (ALE) scheme. Gravitational accelerations are computed using the Tree-PM approach, where long-range forces are calculated with a Fourier particle-mesh

method, medium-range forces with a hierarchical tree algorithm (Barnes & Hut 1986), and short-range forces with direct summation (as in Springel 2005). A local, predictor-corrector type, hierarchical time stepping method obtains second order accuracy in time. Numerical parameters tangential to our current investigation – for example, related to mesh regularization or gravitational force accuracy – are detailed in Springel (2010) and Vogelsberger et al. (2012).

We include a redshift-dependent, spatially uniform, ionizing UV background field (Faucher-Giguère et al. 2009). Gas loses internal energy from optically thin radiative cooling assuming a primordial H/He ratio (Katz et al. 1996). The production of metals and metal line cooling contributions are not included.Star formation and the associated ISM pressurisation from unresolved supernovae are included with an effective equation of state modelling the ISM as a two-phase medium, following Springel & Hernquist (2003). Gas elements are stochastically converted into star particles when the local gas density exceeds a threshold value of $n_{\rm H} = 0.13$ cm^{-3}. Furthermore, there is no resolved stellar feedback that would drive galactic-scale winds, nor any treatment of black holes or their associated feedback. All of the simulations considered in this work disregard the possible effects of radiative transfer, magnetic fields, and cosmic rays. The set of implemented physics is essentially identical to the 'moving mesh cosmology' paper series as described in Nelson et al. (2013).

We identify dark matter haloes and their gravitationally bound substructures using the SUBFIND algorithm (Springel et al. 2001; Dolag et al. 2009) which is applied on top of a friends-of-friends cluster identification. We refer to the most massive substructure in each FoF group as the halo itself. Merger trees are constructed using the SUBLINK code (Rodriguez-Gomez et al. 2015) to link haloes to their progenitors and descendants at different points in time.

All runs include the Monte Carlo tracer particle technique (Genel et al. 2013) in order to follow the evolving properties of gas elements over time, with five tracers per initial gas cell. This is a probabilistic method, where tracers are exchanged between parents based explicitly on the corresponding mass fluxes. By locating a subset of their unique IDs at each snapshot we can, by reference to their parents at that snapshot, reconstruct their spatial trajectory or thermodynamic history.

In the current work we make limited use of the assembly and accretion histories of the haloes, as determined with the tracer particles and merger trees, respectively. Specifically, we verify the correspondence between haloes at differ-

---
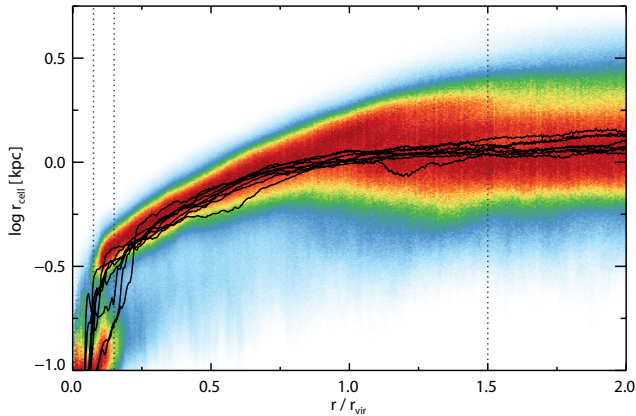[1] http://www.illustris-project.org/files/Nelson15b_ICs.zip

Figure 1. The mass-weighted distribution of gas spatial resolution as a function of radius, for all eight halos stacked together at L11 resolution. As a proxy for spatial resolution, we show the gas cell sphere-equivalent radii $r_{\rm cell}$. Each radial bin is normalized independently, such that the colour mapping reaches its maximum intensity at each radius, independent of the radial distribution of gas mass. The dark vertical lines indicate $1.5\,r_{\rm vir}$, $0.15\,r_{\rm vir}$ and $0.07\,r_{\rm vir}$, the last two bounding the radial range where a density bimodality arises due to the central galaxy. Substructures are excised.

ent resolution levels in order to comment on the convergence properties of our simulations. We reserve as future work – the second paper in this series – a quantitative analysis of the rates and modes of accretion and the impact of merging substructures.

3   RESOLUTION CONSIDERATIONS AND VISUAL INSPECTION

In the vast majority of galaxy formation simulations, spatial resolution is naturally adaptive and follows the hierarchical clustering of structure formation in ΛCDM. This is true for the dark matter, where the Vlassov-Poisson equations are solved with a Monte-Carlo approach. The N-body method is typically used (for notable exceptions see Yoshikawa et al. 2013; Hahn & Angulo 2015). This natural adaptivity also holds for the gaseous component in particle methods like SPH, adaptive grid methods with the typical density-based refinement criteria (for notable exceptions see Iapichino et al. 2008; Rosdahl & Blaizot 2012), and the moving-mesh code used in this work. The resolution is therefore better in collapsed structures than it is in under-dense regions, and maximal in galaxies themselves. The gaseous haloes surrounding galaxies are poorly resolved in comparison, to the extent that modern cosmological simulations (e.g. Khandai et al. 2014; Dubois et al. 2014; Vogelsberger et al. 2014; Schaye et al. 2015) which just barely resolve the internal structure of individual galaxies may be insufficiently capturing gas-dynamical processes in the halo.

We begin by quantifying the spatial resolution of gas in the halo. Figure 1 shows the mass-weighted two dimensional distribution of cell size $r_{\rm cell}$ as a function of radius. As a proxy for the irregular shape of Voronoi polyhedra, we take the sphere-equivalent radius $r_{\rm cell} = (3V_{\rm cell}/4\pi)^{1/3}$ where $V_{\rm cell}$ is the exact Voronoi cell volume. The mesh reg-

ularization scheme ensures that this value is approximately equal to the actual geometrical distance between the generating point and each face centre. All haloes are stacked together at the highest (L11) resolution level, while black lines show the median relation for each halo separately.

Beyond $r/r_{\rm vir} > 1.25$ the hydrodynamic resolution is nearly constant, but with a broad distribution spanning from $\sim 500\,{\rm pc}$ to $\sim 3\,{\rm kpc}$ (physical), depending on what level of overdensity the gas cell resides in. In the halo region, $0.25 < r/r_{\rm vir} < 1.0$ the mean resolution scales from $\sim 400\,{\rm pc}$ up to $\sim 1\,{\rm kpc}$. The inner halo, typically bounded by $r \lesssim 0.15 r_{\rm vir}$ sees the mean cell size decrease rapidly under $\sim 100\,{\rm pc}$ as dense gas features associated with the central galaxy begin to dominate. We return to the implications of the relatively coarse halo resolution in the discussion.

In Figure 2 we show a visual example of the resolution issue and a first look at the impact of higher hydrodynamical resolution in the halo regime. One halo (h0) is included at the three increasing zoom levels considered in this work, L9, L10, and L11, increasing from left to right. On the top row we plot a slice of the Voronoi mesh used to evolve the gas component.[2] The slice is centred on the central galaxy, which lies at the origin, and to focus on details we include only the upper-right quadrant. The outer red circle marks the virial radius of 114 physical kpc at $z = 2$. At all three resolution levels we see that the high-density gas near the origin is resolved at the sub-kpc level and impossible to separate at this scale, while at the virial radius individual gas elements are substantially larger. At L9, characteristic of modern cosmological simulations, the virial arc across a quadrant is only resolved by $\simeq 20$ cells, while the radial structure between $0.5\,r_{\rm vir}$ and $1.0\,r_{\rm vir}$ is only resolved by $\simeq 10$ cells. This is roughly consistent with a zeroth order estimate, assuming uniform density, for a number of cells per dimension of

$$N_{\rm cell,dim} \sim \left(\frac{(\Omega_b/\Omega_m) \times M_{\rm halo}}{m_{\rm cell}} \right)^{1/3} \simeq 50 \qquad (1)$$

which are available to resolve the halo gas structure of a $10^{12}\,{\rm M}_\odot$ halo. At L11 this increases to $N_{\rm cell,dim} \simeq 250$, but the scaling is obviously slow in three-dimensions. In the discussion we consider a possible method for improving upon this resolution issue in the halo with future work.

Across the bottom row we show a projection of mass-weighted gas temperature, where the colormap extends from cold, $\sim 10^4\,{\rm K}$ gas as blue to hot, $\sim 10^6\,{\rm K}$ gas as red. Some interesting differences emerge as the gas resolution in the halo increases. The large cold inflow which begins to experience substantial heating at $(0.4 - 0.5) \times r_{\rm vir}$ shows some temperature inhomogeneities at L9, but is essentially a single coherent structure. At L10, this inflow is resolved into a number of smaller gas filaments by the time it crosses half the virial radius. At L11 the temperature structure becomes even more complex, throughout the halo, with small scale features emerging below the cell-size of the lower resolution

---

[2] Note that the intersection of a plane with the three-dimensional Voronoi tessellation does not in general produce a two-dimensional Voronoi graph. Therefore the shapes of individual cells, as shown, do not reflect the actual regularity of the computational mesh.
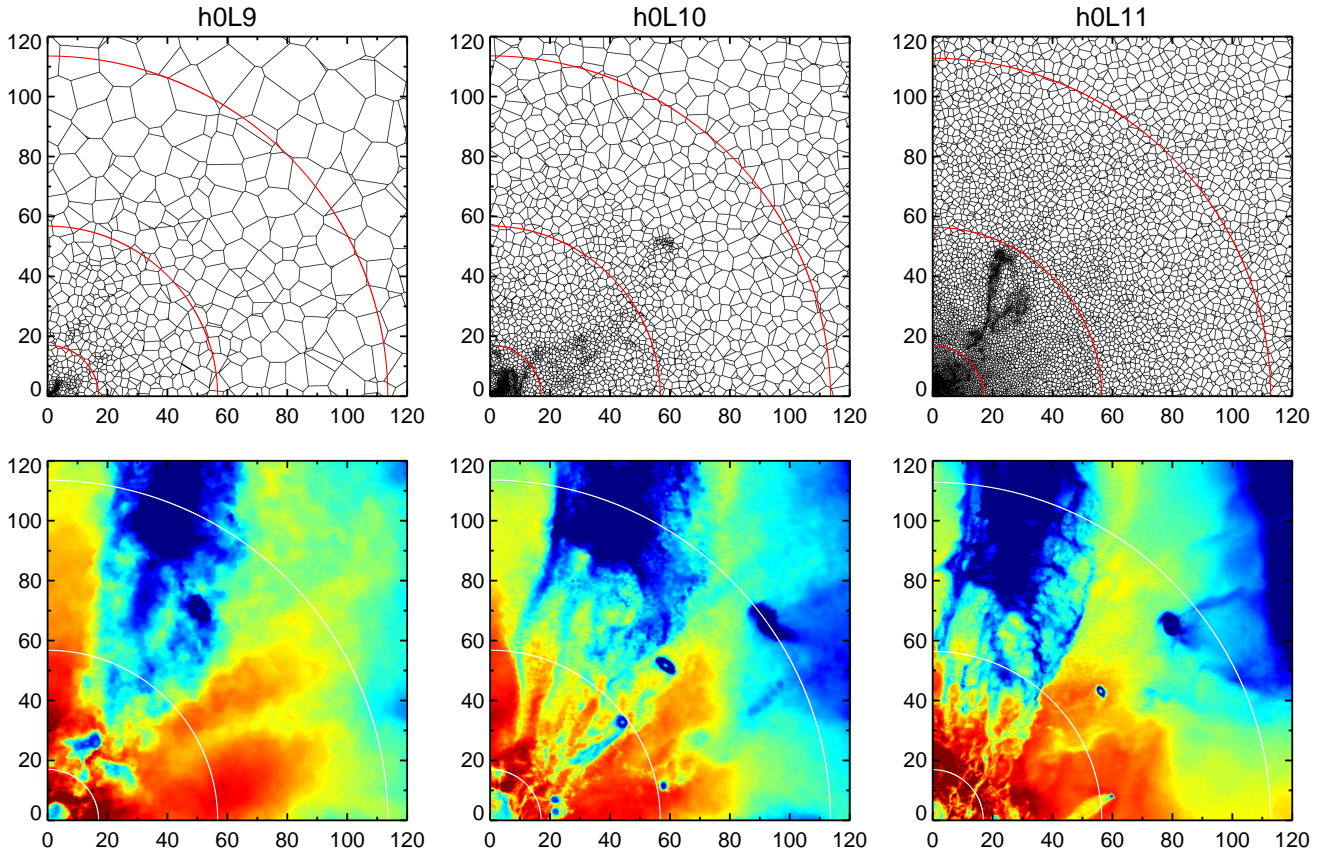
Figure 2. Slice through the Voronoi mesh showing the underlying spatial discretization (top) and a projection through the linearly reconstructed, mass-weighted gas temperature field (bottom) with $\sim 10^4$ K as blue and $\sim 10^6$ K as red. Halo h0 is shown at $z = 2$. We include only the upper right quadrant, after centring the halo at the origin, in orthographic projection. The circles denote $\{0.15, 0.5, 1.0\}\,r_{\rm vir}$, the axes units are in physical kpc, and the projection depth is 238 kpc. The average gas cell size near the virial radius drops with increasing spatial resolution (from left to right), from $\sim$2.7 kpc to $\sim$0.8 kpc physical. Note that the exact state of gas in the halo, and the location of satellites, differs somewhat due to timing offsets between the three runs.

runs. Clearly the morphology of accreting gas and its interaction with the quasi-static hot halo material depends on numerical resolution to some degree. In the following sections we further investigate this dependence by analysing the structure of halo gas at our highest available resolution.

3.1 Visual Inspection

We present a visual overview of the eight simulated haloes at $z = 2$, focusing on the virial scale of haloes 0-3 in Figure 3, and of haloes 4-7 in Figure 4, one halo per row. In each case, we show mass-weighted projections of gas density, temperature, entropy, and radial velocity in each column (left to right). All gas cells within a cube of side-length $3\,r_{\rm vir}$ are included, while the temperature of star forming gas on the effective equation of state (eEOS) is set to a constant value of 3000 K. The three concentric circles denote $\{0.15, 0.5, 1.0\} \times r_{\rm vir}$.

We have separated the eight systems into two groups based roughly on the morphology of their halo gas – the first four haloes (h0-3) are closer to equilibrium at $z = 2$ and the structure of their hot gas is roughly spherical, whereas

the second four (h4-7) are significantly more disturbed. In the first case, the virial shock can be clearly seen as a sharp increase to higher temperature and entropy, typically at $\gtrsim 1.25\,r_{\rm vir}$. However, the radius of the shock (see also Schaal & Springel 2015) or its existence at all depends strongly on direction, which we explore further in Section 5. These boundaries are also associated with a decreased inflow velocity – that is, radial stalling – as well as increased gas density.

At $z = 2$ haloes at this mass scale of $\simeq 10^{12}\,{\rm M_\odot}$ typically reside at the intersection of multiple large-scale filaments (and/or sheets) of the cosmic web. This naturally leads to a significant amount of filamentary inflow across the virial radius. We see that these inflows cover only a fraction of the virial sphere. They can maintain coherency to at least half the virial radius while maintaining a strong overdensity with respect to the mean gas density at each radius. They experience significant heating, typically at $\sim 0.5\,r_{\rm vir}$, from $\lesssim 10^{4.5}$ K to $\gtrsim 10^6$ K, reaching the peak temperature of the mean $T_{\rm gas}(r)$ in the inner halo. Their entropy can remain lower than that of the hot halo gas at these radii, $\sim 10^{8.0-8.5}\,{\rm K\,cm^2}$ compared to $\sim 10^9\,{\rm K\,cm^2}$. Although the
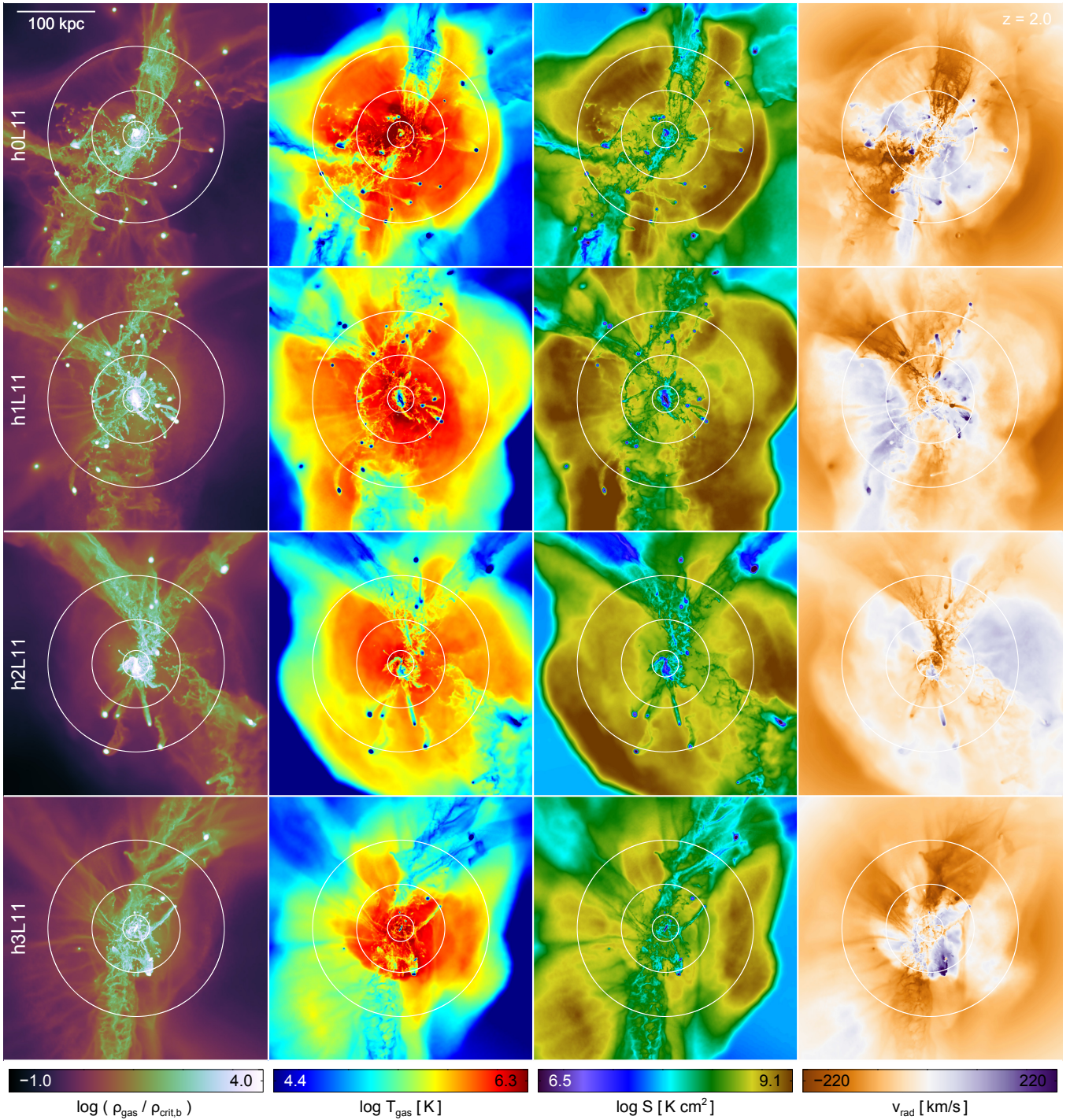
Figure 3. Mass-weighted projections of gas density, temperature, entropy, and radial velocity for the first four simulated haloes at $z=2$. In each case, all gas cells within a cube of side-length $3\,r_{\rm vir}$ are included, and distributed using the standard cubic spline kernel with $h = 2.5\,r_{\rm cell}$ in orthographic projection. The white circles denote $\{0.15, 0.5, 1.0\}\,r_{\rm vir}$. Gas density is normalized to the critical baryon density at $z=2$. The temperature of star forming gas on the eEOS is set to a constant value of $3000\,{\rm K}$.

mean radial velocity inside the halo is generally near equilibrium/zero (denoted by white in the colormap), we see that in a given direction this is rarely the case, finding instead either non-negligible inflow or outflow velocities.

Two haloes, h3 and h7, have a large number of small, prominent, inflowing streams in the radial range $0.5r_{\rm vir} \lesssim r \lesssim 1.25r_{\rm vir}$ (see density maps). They originate from the

lower left direction in the case of h3, and from the top for h7. These filaments are not associated with large-scale structure, and have characteristics distinct from the much larger filaments which are associated with features at larger radii. In particular, although they obtain similarly high inflow velocity, their entropy and temperature are above that of the IGM, and their overdensity with respect to the radial
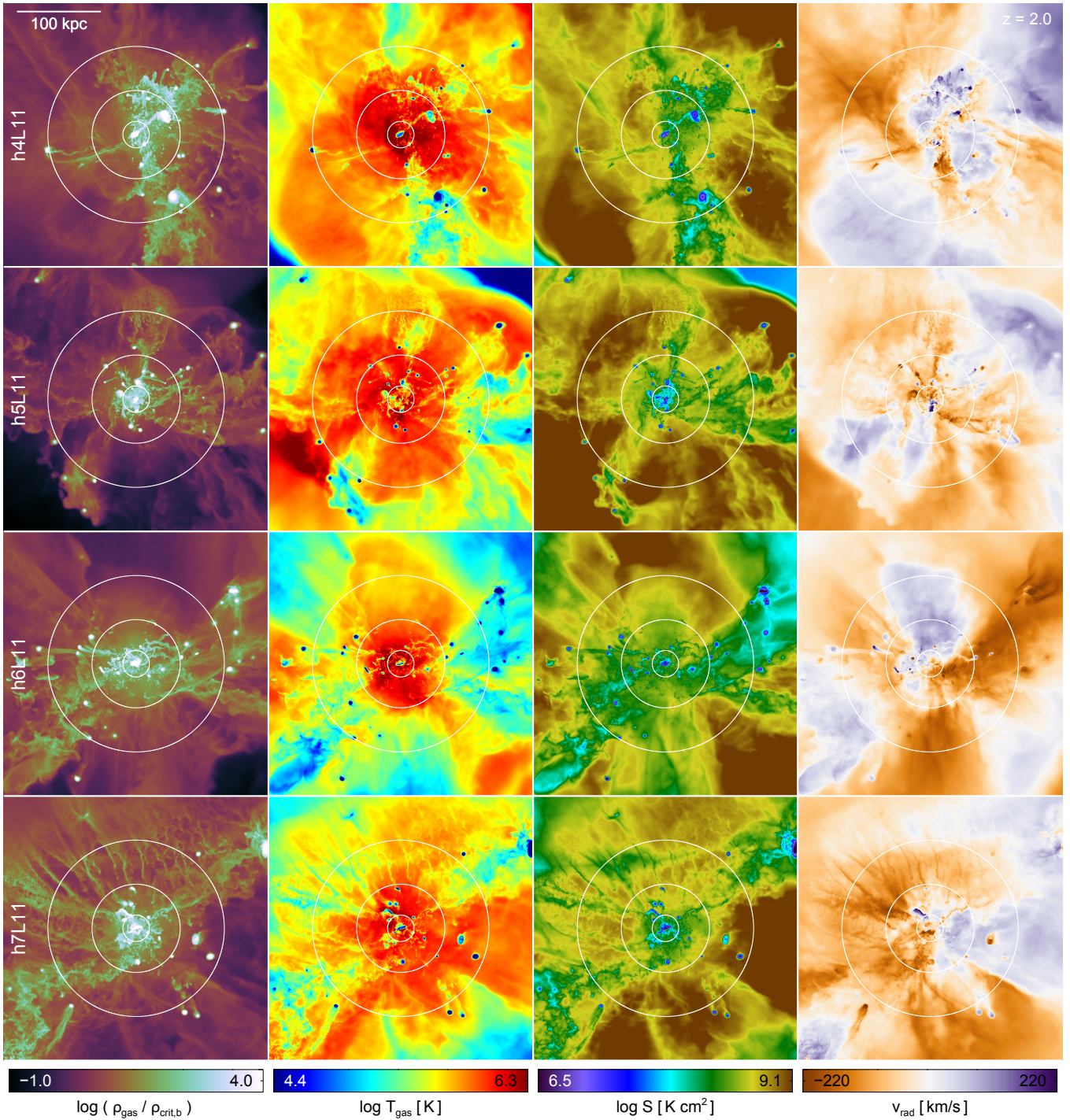
Figure 4. As in the previous figure, mass-weighted projections of gas density, temperature, entropy, and radial velocity at $z = 2$, but for the other four simulated haloes.

mean is not as significant. Some of the other six haloes exhibit similar features at various points in the past, but they have disappeared by $z = 2$. In general, we observe that these features form between one and two times the virial radius semi-spontaneously, as in an instability, commonly triggered by perturbations either from substructure debris or the intersection of sheet-like structure in the cosmic web. They are marginally evident at L10 and absent at L9. We reserve

an in-depth analysis of the formation of these features and whether or not their growth corresponds to a physical instability in the gas for future work.

We visualize two additional scales, the inner halo structure as well as the large-scale context, of the eight simulated haloes at $z = 2$. Figure 5 includes haloes 0-3 while Figure 6 includes haloes 4-7. The left two columns show the projected density of the gas and stellar components, the white circles
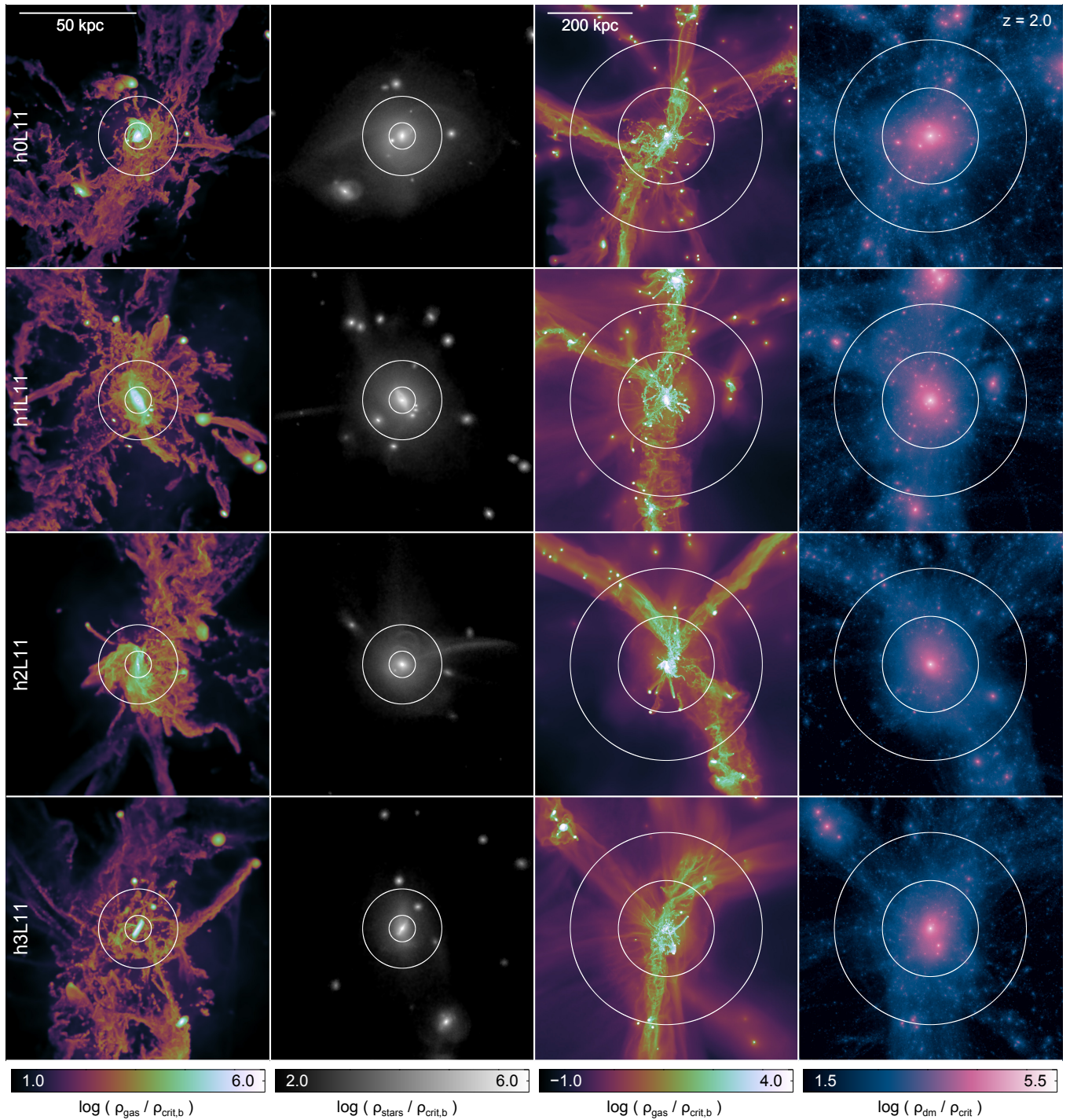
Figure 5. Mass-weighted projections of gas and stellar density temperature at small scales (left two columns), and projected gas density and dark matter density at large scales (right two columns). The first four simulated haloes are shown at $z = 2$. All gas cells or particles within a cube of side-length $1.0\, r_{\rm vir}$ (small scales) or $5.5\, r_{\rm vir}$ (large scales) are included, and distributed using the standard cubic spline kernel with $h = 2.5\, r_{\rm cell}$ (gas) or $h = r_{32,\rm ngb}$ (the radius of the sphere containing the 32 nearest neighbours of the same particle type, for stars and dm) in orthographic projection. The white circles denote $\{0.05, 0.15\}\, r_{\rm vir}$ (left two columns) and $\{1, 2\}\, r_{\rm vir}$ (right two columns). Densities are normalized to the critical (baryon) density at $z = 2$.

indicating $0.05\, r_{\rm vir}$ and $0.15\, r_{\rm vir}$. The right two columns show the projected density of the gas and dark matter components, the white circles here indicating $1.0\, r_{\rm vir}$ and $2.0\, r_{\rm vir}$.

In the centre of the halo, $r/r_{\rm vir} \lesssim 0.3$, the gas component forms a complex morphology with multiple orbit-

ing substructures, commonly associated with tails and gas streams from ram-pressure stripping, as well as tidally-induced bridges and spiral patterns. Rapidly varying velocity fields modulate inflowing as well as outflowing material. At $r/r_{\rm vir} \lesssim 0.05$ a large gas disc is a common feature –
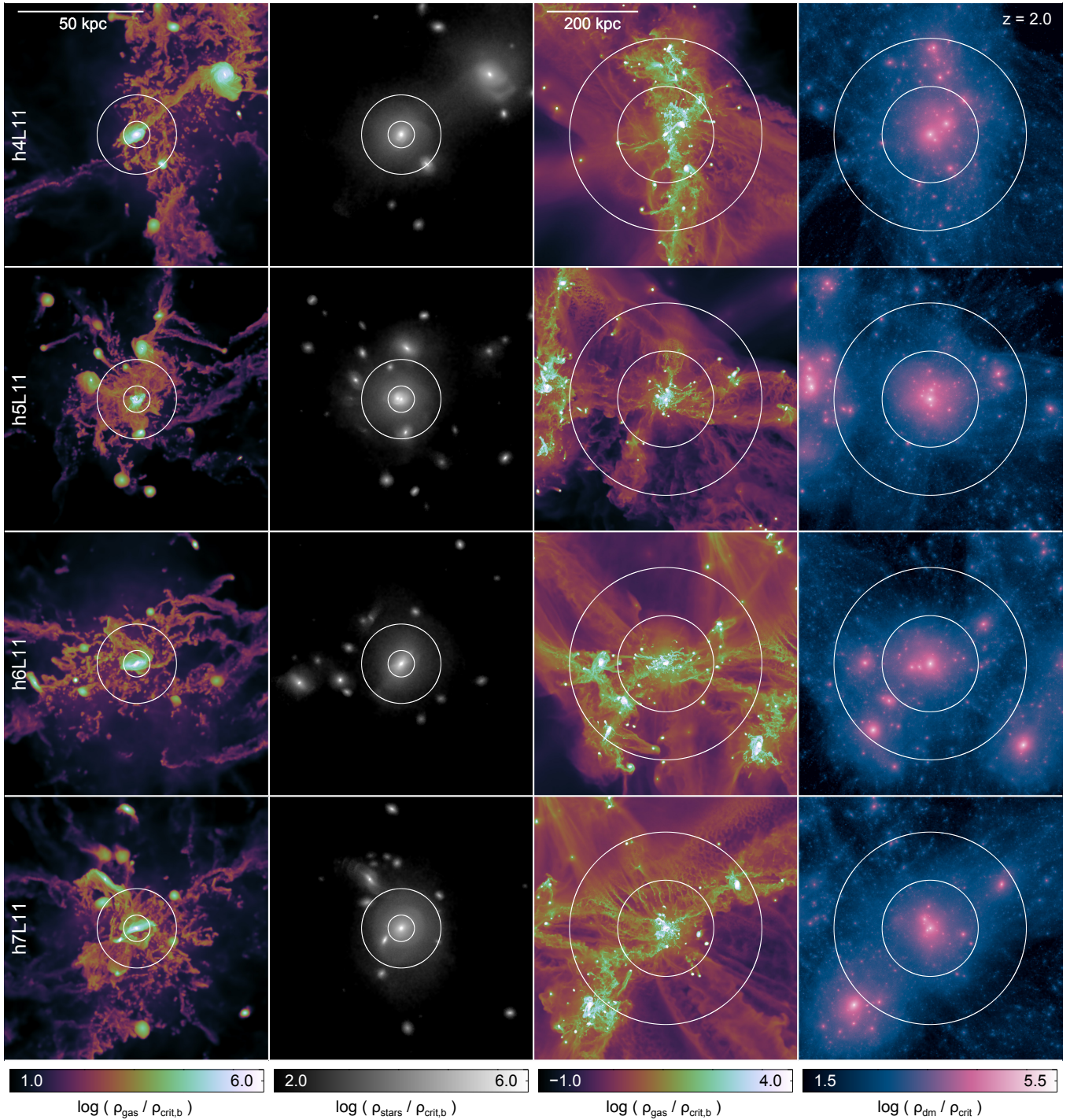
Figure 6. As in the previous figure, projections of gas and stellar density on small scales (left two columns), and gas density and dark matter density on large scales (right two columns) at $z=2$, but for the other four simulated haloes.

the final stage in the transformation from large-scale structure and the associated tidal torques to the formation of a galaxy. Here the coherent angular momentum of the halo as a whole must transition to the angular momentum of the forming disc through the complicated dynamics of this inner halo 'messy' region (Danovich et al. 2014). In the small-scale views of h2 we see tidal features in the collisionless stellar distribution (extending to the right from the centre), with-

out any corresponding structure in the gas. In h3, we see a massive tidal tail in gas extending out to $\simeq 0.5 r_{\rm vir}$ (towards upper right of panel), with no corresponding structure in the stars. A recent post-pericenter passage of an ongoing major merger in h4 has induced tidal features in the large companion (upper right of figure) which is still on an outgoing orbit, and generated a long tidal tail, of which the inner half has reversed direction and is falling back on to the central

galaxy. A recent merger in h5 has left a double nucleus in the stars, separating by roughly one kpc. In h7 we see a strong tidal warp in the gas and stars of the merging companion (to the upper left of the central), with several stellar shells from earlier minor mergers superimposed. In general, we can see that many of the narrow inflowing streams in the inner halo are tidal in nature, which highlights the importance of characterizing the origin of gas accretion features – this component of the accretion rate would have been characterized as a 'stripped' component in the methodology of Nelson et al. (2015).

In the inner regions of the halos which we have identified as in equilibrium, the perturbations and gas structures generated by the dynamics of satellite galaxies (see Zavala et al. 2012) are superimposed on a gas background which is aligned at Mpc scales with large-scale gas features. For example, the broad inflow in h0 (towards the top of the image panel) with a width of ~ 50 kpc at $0.5\,r_{\rm vir}$ is clearly associated with a gas overdensity extending out to at least $3\,r_{\rm vir}$. Likewise for the broad inflow in h2 (also, top of the image panel) which has coalesced at the intersection of two such cosmic web filaments. These inflows are not smooth features of constant density gas. They have a 'wavy' or rippled appearance, arising from gas density contrasts as high as a factor of $\sim 10^3$. By visual inspection it is clear that, at least at sufficient resolution, such inflowing filaments are in fact associations of multiple smaller structures with coherent kinematics and origin.

The second set of haloes (h4-7), which are in general more morphologically disturbed, do not show this clear association between small-scale and large-scale gas features. Their time evolution indicates that this is often a consequence of a major halo-halo merger where the two gas reservoirs collide and disrupt any radially coherent gas kinematics as the hot halo re-equilibrates. However, recent major mergers are not always seen, and the nearby environment and topology of large-scale structure also appear to play a significant role in the sphericity of halo gas, independent of assembly history. For example, we consider the number of major mergers with ratio $\eta \geqslant 1/3$ experienced by each halo while the stellar mass is greater than $10^{10.5}\,{\rm M_\odot}$ (roughly $2 < z < 4$), as well as the maximum merger ratio of any merger, under the same constraint. In both cases, the mass ratio is determined at the time the less massive progenitor reaches its maximum stellar mass (see Rodriguez-Gomez et al. 2015). We find that h0, h2, and h3 have had no major mergers exceeding this mass ratio, and indeed none with $\eta \geqslant 0.2$. The outlier is h1, which did have one major merger ($\eta = 0.8$). In the disturbed group, h4 has had four major mergers ($\eta_{\rm max} = 0.6$), h6 has had one ($\eta = 0.65$), and h7 has had three ($\eta_{\rm max} = 0.95$). The outlier is h5, which has had no major mergers satisfying this criterion, the largest mass ratio being $\eta = 0.2$.

4   THE PHYSICAL STATE OF HALO GAS

In this Section, we quantify the gas behaviours noted above, first by giving the spherically-averaged profiles of gas density, cell size, temperature, entropy, radial velocity, and specific angular momentum, and then by examining the pairwise correlation matrix of these same gas quantities.

4.1   Characteristic Halo Properties

In what follows we will normalize the distance of gas cells from the halo centre by the virial radius, as calculated for each halo at each resolution. For simplicity, we will in general not normalize the thermodynamic properties of gas since our halo mass range is so narrow. Instead, to provide a sense of reference, we calculate representative values for gas temperature, entropy, density, velocity, and angular momentum for a halo of $M_{\rm halo} \simeq 10^{12}\,{\rm M_\odot}$ at $z = 2$. Numerical values are given here. First, we take the virial temperature as

$$T_{\rm vir} = \frac{\mu m_p v_{\rm vir}^2}{2k_B} \simeq 10^{6.3}\,{\rm K} \qquad (2)$$

following Barkana & Loeb (2001), where $\mu \simeq 0.6$ for a fully ionized, primordial gas. We take entropy as $S = P/\rho^\gamma$ where pressure is $P = (\gamma - 1)T\rho$. A virial entropy is then defined as

$$S_{\rm vir} = \frac{P_{\rm vir}}{\rho_{vir}^\gamma} = (\gamma - 1)T_{\rm vir}\rho_{\rm vir}^{(1-\gamma)} \simeq 10^{8.0}\,{\rm K\,cm^2} \qquad (3)$$

where we have taken $\rho_{\rm vir} = 200(\Omega_b/\Omega_m)\rho_{\rm crit}(z)$, the baryon fraction multiplied by two hundred times the critical density of the universe at that redshift. Using the chosen overdensity criterion, the virial radius is then

$$r_{\rm vir} = \left(\frac{GM_{\rm halo}}{100H(z)^2} \right)^{1/3} \simeq 100\,{\rm kpc} \qquad (4)$$

in physical units, while the virial velocity is

$$v_{\rm vir} = \sqrt{\frac{GM_{\rm halo}}{r_{\rm vir}}} \simeq 205\,{\rm km/s}. \qquad (5)$$

Finally, for the specific angular momentum of the halo we take

$$j_{\rm vir} = \sqrt{2}\lambda v_{\rm vir}r_{\rm vir} \simeq 10^{3.0}\,{\rm kpc\,km/s} \qquad (6)$$

using a spin parameter of $\lambda = 0.035$ (Barnes & Efstathiou 1987; Bullock et al. 2001). These characteristic values for the temperature, density, entropy, radial velocity, and specific angular momentum of the halo gas are typically reached at some reasonable fraction of the virial radius, e.g. $\sim (0.1 - 0.5) \times r_{\rm vir}$. We use them below to provide a useful reference with which to identify halo gas in different physical states.

4.2   Radial Gas Profiles

In Figure 7 we show the median radial profiles of six gas quantities: temperature, density, radial velocity, cell size, entropy, and specific angular momentum. The main panel plots the profile for each of the eight haloes individually (different line colours) at the L11 resolution level. Light colours are used to indicate the four 'equilibrium' haloes, while darker colours indicate the four more 'disturbed' systems. The subpanels show the ratio of the radial profiles comparing the L9/L11 and L10/L11 runs, where the thick black lines indicate the average across haloes. We have excised all gravitationally bound substructures before constructing mean radial profiles, which would otherwise appear as a forest of small, dense, cold systems in these figures. A few observationally and theoretically motivated scalings with radius are included for reference (dotted and dashed lines).
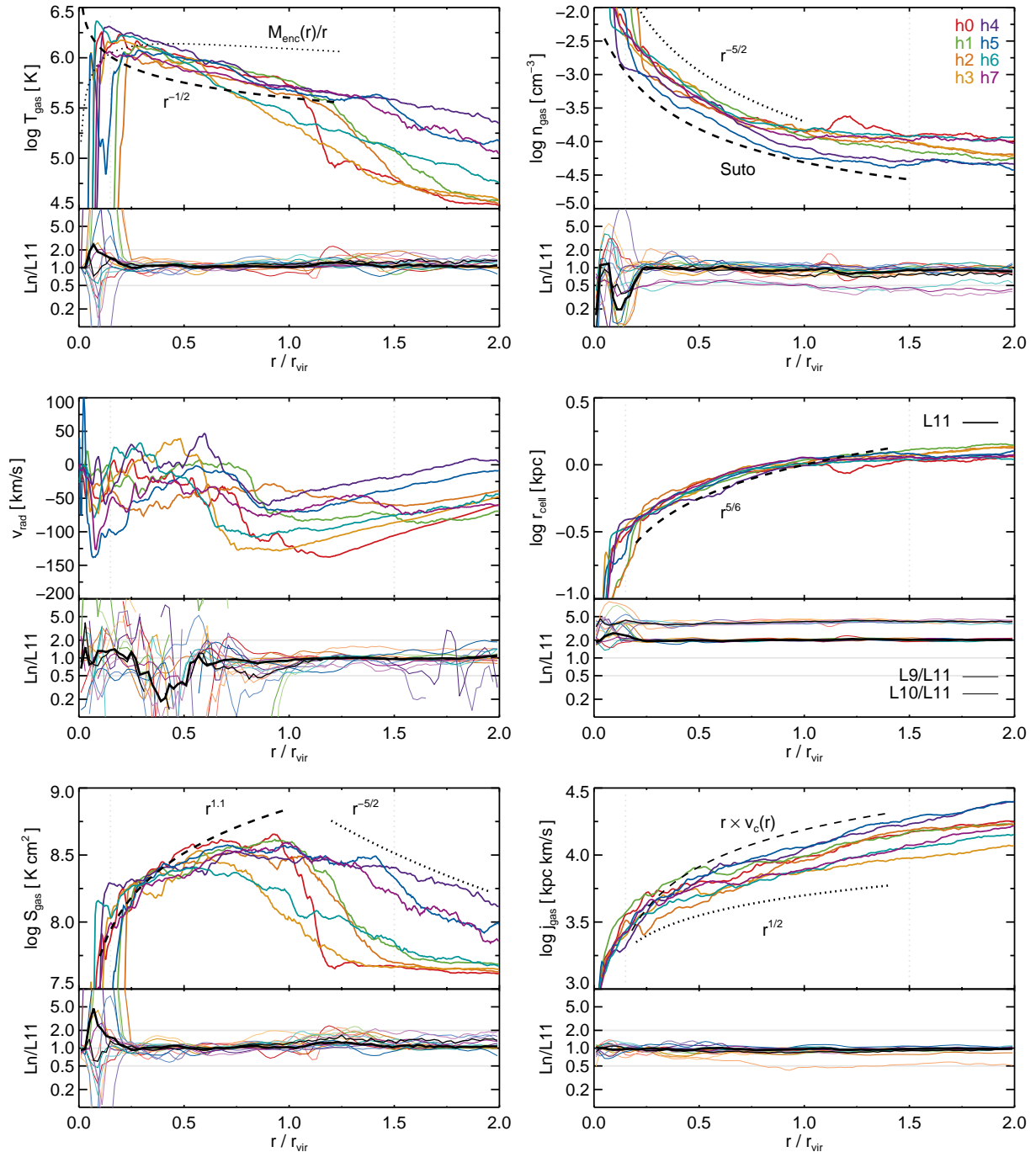
For instance, going beyond an isothermal model for gas

Figure 7. The median radial profiles of six quantities: gas temperature, density, radial velocity, cell size, entropy, and angular momentum. Each halo is shown separately (by colour). The main panels for each quantity show the highest resolution only, while the subpanels show the ratio of the two lower resolution runs to L11 (the mean ratios across all eight haloes are indicated with thick black lines). Various scalings with radius are provided for reference (dotted and dashed lines). All gas within $2r_{\rm vir}$ is included, except that substructures are excised.

temperature, we can take a gas component tracing dark matter distributed according to a NFW profile. This leads to a scaling of $T_{\rm gas} \propto M_{\rm enc}(r)/r$ (e.g. Makino et al. 1998), which is still much too shallow (dotted line). Instead for $r/r_{\rm vir} \gtrsim 0.15$ we have approximately $T_{\rm gas} \propto r^{-1/2}$. Of all eight systems, h0 exhibits the sharpest temperature drop defining an outer boundary of the halo at $r \simeq 1.2 r_{\rm vir}$, while

in most cases there is no sharp transition at or near the virial radius. In all cases the temperature drops precipitously in the inner halo, at 5%-10% of $r_{\rm vir}$. Note that we have assigned a gas temperature of 3000 K to gas on the star-forming equation of state, which would otherwise have an artificially high effective temperature. The $T_{\rm gas}(r)$ profiles are well converged with resolution. The mean across

all eight haloes and averaged over $0.15 < r/r_{\rm vir} < 1.5$ is L9/L11 $\simeq 1.15$ and L10/L11 $\simeq 1.08$, while at the largest radii the lower resolution runs have mean temperatures biased high by up to $\simeq 30\%$. Physics will dominate resolution – different models for galactic-scale stellar winds or AGN feedback can substantially modify the mean gas temperature profile inside as well as outside $r_{\rm vir}$ (Suresh et al. 2015).

A gas density scaling as $n_{\rm gas} \propto r^{-5/2}$ approximates the mean behaviour of the haloes well, as does a model for an isothermal gas in hydrostatic equilibrium (Suto et al. 1998, using $B = (n+1)B_p$ with $n = 7$, $B_p = 1$). However, the other panels make it clear that the gas is not in hydrostatic equilibrium, nor isothermal, implying this agreement may be coincidental. Convergence at lower resolutions is reasonable – over the same radial range we find L9/L11 $\simeq 0.8$ and L10/L11 $\simeq 0.9$, indicating that the mean gas densities are lower in the lower resolution runs. This is potentially a consequence of better resolving satellite galaxies and their interactions with the central host, which fills the halo volume with more high density gas cells. These are no longer instantaneously bound to the satellite, and so are not excluded. [3] The total halo gas mass actually decreases somewhat at higher resolution ($\sim 10\%$ or $\sim 5\%$ lower for L11 as compared to L9 or L10, respectively), which would otherwise modify gas densities in the opposite direction. Finally, the variable assembly histories lead to the large halo-to-halo scatter, while the sensitivity of merger states to temporal offsets driven by short dynamical time-scales leads to large scatter between resolution levels. As with temperature, however, the caveat is that radial density profiles will depend in detail on the implemented feedback models (Hummels et al. 2013).

We see a similar scatter in the Hubble-corrected gas radial velocities. The haloes have different velocity structures, which commonly feature a slowly increasing inflow velocity down to $\sim 0.75\,r_{\rm vir}$, at which point there is a noticeable bump towards an equilibrium value of $v_{\rm rad} \simeq 0\,{\rm km/s}$. Until reaching the central galaxy, the radial velocity profiles are then roughly flat. In the following discussion of Figure 8, however, we show that the mean (or median) velocity profile is an exceedingly poor representation of the dynamics of halo gas. For example, in the mean the quasi-static halo rarely has $v_{\rm rad} > 0$ for $0.15 < r/r_{\rm vir} < 1.0$, while in actuality this value is driven down by the superposition of rapidly inflowing and gently outflowing components.

The gas spatial resolution, for which we again use the sphere-equivalent radii $r_{\rm cell}$ as a proxy, becomes better with decreasing radius as expected. Given our constant cell mass refinement criterion, it scales roughly as the cube-root of the density scaling. That is, $r_{\rm cell} \propto V_{\rm cell}^{1/3} = (m_{\rm cell}/\rho_{\rm cell})^{1/3} \propto \rho_{\rm cell}^{-1/3}$. At L9 and L10 the cell sizes are a factor of four and two larger, respectively, scaling with the mean inter-cell spacing as $r_{\rm cell} \propto L_{\rm box} N_{\rm cell,tot}^{-1/3}$.

We overplot the gas entropy profiles with the near-linear scaling $S_{\rm gas} \propto r^{1.1}$ often seen in x-ray observations of local clusters (e.g. George et al. 2009). Despite looking at the significantly more massive cluster PKS 0745-191,

$\sim 10^{14}\,{\rm M}_\odot$ in the nearby universe ($z \simeq 0.1$), the inferred radial characteristics from George et al. (2009) are in reasonable agreement with the haloes simulated in this work. A similar level of qualitative agreement is evident at $z = 2$ for $\sim 10^{12}\,{\rm M}_\odot$ haloes in gas temperature, entropy, and density with previous cosmological simulations at L8-equivalent resolution and incorporating more realistic feedback physics (van de Voort & Schaye 2012). In both cases, entropy rises to near the virial radius at which point it flattens and becomes roughly constant. While some haloes exhibit this gradual plateau (h4), the radial entropy profile of others drops as r^{-2} or faster (h2) at some radius $\geqslant r_{\rm vir}$. There is a correspondence between the equilibrium state of the halo and its properties beyond the virial radius – the more disturbed systems (h4-7, darker line colours) generally have higher entropy, without any strong transition. The entropy profiles, averaged over all eight haloes, are well converged with respect to L9 and L10. [4]

The specific angular momentum scales roughly as $r^{1/2}$ or even more accurately as $j_{\rm gas} \propto r\,v_c(r)$ given the circular velocity $v_c(r) \propto (M_{\rm enc}(r)/r)^{1/2}$ for an NFW profile of this halo mass. There is broad uniformity among the eight haloes and good convergence in the lower resolution runs, with a small systematic bias towards lower angular momentum content in the halo, L9/L11 $\simeq 0.88$ and L10/L11 $\simeq 0.96$, again driven by high velocity tidal debris becoming better resolved at the highest resolution.

4.3   Distributions Beyond Radial Dependence

To avoid missing important features by averaging over multiple gas populations with distinct properties residing at similar radii, we examine the two dimensional distributions of these same gas quantities. Instead of only considering their radial dependence, in Figure 8 we show a full pairwise correlation matrix, every quantity plotted with respect to every other. Here we have stacked together all eight haloes at L11, normalizing only the radius of each gas cell with respect to $r_{\rm vir}$ of its parent halo. Despite the different thermal and dynamical structures of the haloes we verify that the key features seen individually in each are preserved in this collective view. To explore the various relations, we have separately normalized each panel 'column by column'. That is, for each value along the x-axis, the colour mapping of the corresponding one dimensional, vertical slice is independent, such that each slice extends from low values (white/blue) through intermediate values (green/yellow) to high values (orange/red). Therefore, there is no global indication of the distribution of mass within each panel (although very noisy regions indicate a poor sampling and therefore comparably little gas mass). In addition, the corresponding panels across the diagonal are not just transpositions of one another, but answer different questions. For example, the $T_{\rm gas}(r)$ panel in the first column indicates, for each radius, the dominant temperature(s) of gas at that radius, whereas the $r(T_{\rm gas})$

---

[3] The filamentary feature in the upper right panel of Figure 2, extending from $\simeq 0.15\,r_{\rm vir}$ to $\simeq 0.5\,r_{\rm vir}$ is an example of such a tidal tail.

[4] In the inner halo, h1 and h2 have sharp drops in both $T_{\rm gas}$ and $S_{\rm gas}$ at a larger radius than typical, $\sim 0.25\,r_{\rm vir}$. In these two cases, while the profiles are properly centred on the galaxy, the galaxy is not entirely centred within the halo. This leads to more cold, low entropy gas beyond the typical disc size.
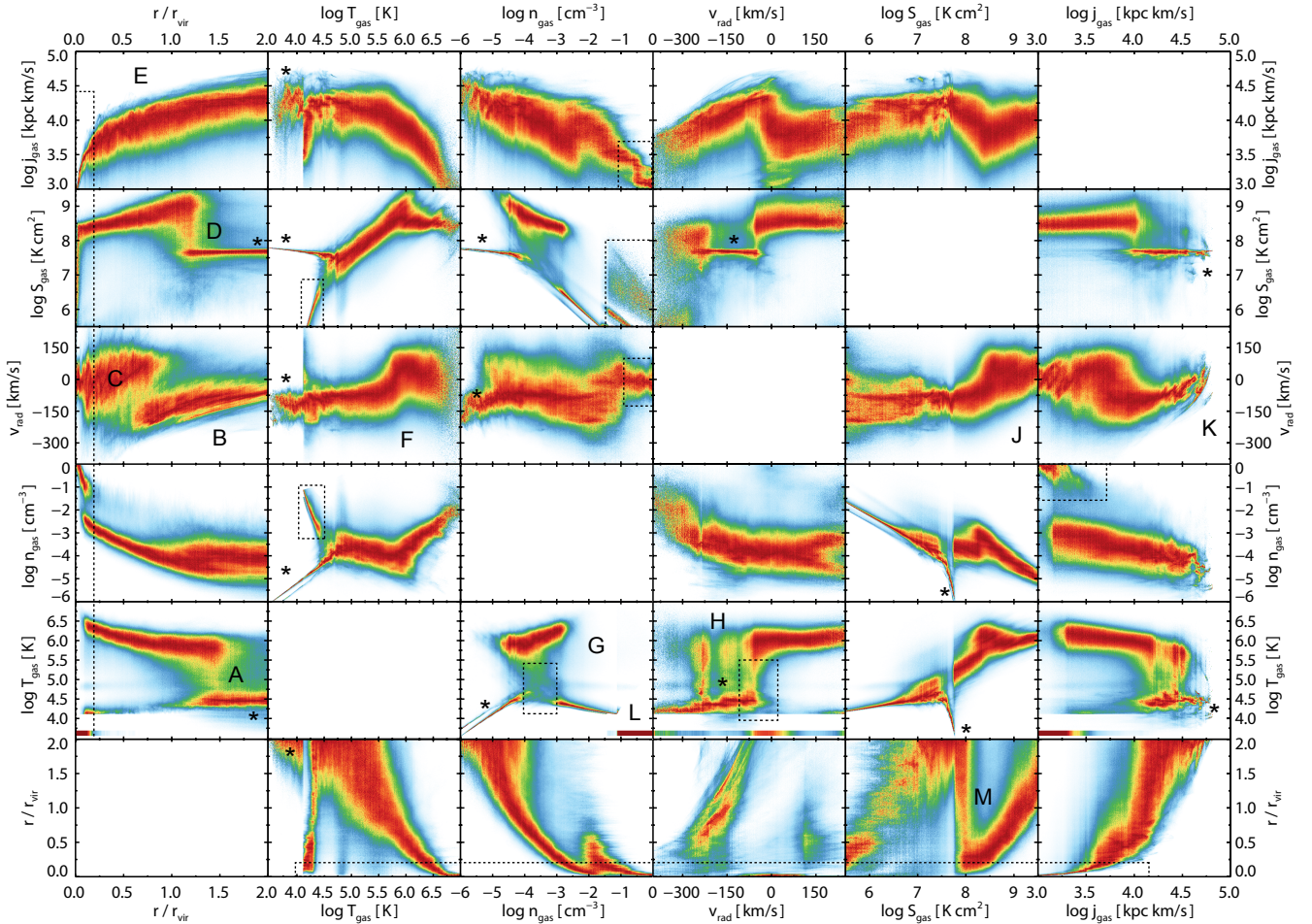
Figure 8. The mass-weighted, two dimensional correlation matrix between all pairwise combinations of six quantities: gas radius, temperature, density, radial velocity, entropy, and angular momentum. All eight halos are included and stacked. Each radial bin is normalized independently, such that the colour mapping reaches its maximum intensity at each x-value, independent of the radial distribution of gas mass. Therefore, panels symmetrically across the diagonal from one another are not simply transpositions, but include additional information. Substructures are excised.

panel in the second column indicates, for each temperature, the dominant radius (or radii) of gas with that temperature. We describe some of the more interesting features seen in this matrix, which have been labelled with letters (A)-(M).

- (*) Denotes features which arise in the intergalactic medium and disappear if gas at $r > r_{\rm vir}$ is excluded. In particular, all the strong constant entropy features at $S_{\rm gas} \simeq 10^{7.7}\,{\rm K\,cm^2}$ in the second row from the top, and the near-discontinuities at this same value in the second column from the right.

- ☐ Regions demarcated with dotted rectangles indicate features arising in the galactic disc or its vicinity, and disappear if gas at $r < 0.2 r_{\rm vir}$ is excluded. This includes all low j gas at high density, which is already above the threshold for star formation in the galaxy. It also includes low temperature gas which has a radial velocity near zero, as well as the thin horizontal feature of $v_{\rm rad}$ spanning $\sim 0 \pm 100\,{\rm km/s}$ near $r = 0$ corresponding to a rotating disc. Interestingly, the prominent temperature bridge between the hot halo and galaxy at intermediate densities also largely disappears, in-

dicating that a majority of this cooling occurs at $r < 0.2 r_{\rm vir}$ (see also G).

- (A) The virial shock seen as a sharp temperature jump from $T_{\rm IGM} \sim 10^{4.5}\,{\rm K}$ to $\sim 10^{6}\,{\rm K}$. The width of this transition varies greatly between the eight haloes, h0 being the narrowest at $\Delta r/r_{\rm vir} \simeq 0.1$, and as seen here in the stack broadened to $\Delta r/r_{\rm vir} \simeq 0.5$ or more. The radius where this transition occurs is typically between $1.25\,r_{\rm vir}$ and $1.5\,r_{\rm vir}$. After shocking, the temperature slowly increases with radius, following the mean radial profile of the halo, until it reaches $\sim 0.25 r_{\rm vir}$ where higher densities lead to accelerated radiative cooling, allowing gas to join the cold ISM phase.

- (B) The radial velocity profile of inflowing gas. This component speeds up as it flows in from large distances down to $\sim 0.5 r_{\rm vir}$ at which point it largely disappears. The mean velocity is approximately -75 km/s at $2\,r_{\rm vir}$, -150 km/s at $r_{\rm vir}$, and -225 km/s at $r_{\rm vir}/2$. For free-fall from rest at infinity to a point mass of $10^{12}\,{\rm M_\odot}$ we would expect a speed of -200 km/s at twice the virial radius. The actual value is less due the combination of the Hubble expansion and gas dynamics. Given this offset at the halo outskirts, the subsequent scaling is roughly consistent with $v_{\rm rad} \propto r^{-1/2}$ as

expected from free-fall, at least down to $\sim 0.5\,r_{\rm vir}$, below which inflow no longer dominates by mass.

• (C) The radial velocity distribution of the hot halo gas. These two components overlap between $0.5 < r/r_{\rm vir} < 1.0$ as gas transitions from rapidly inflowing to quasi-static. It really is 'quasi', however, since a large mass of gas has positive radial velocity. Gas with $v_{\rm rad} > 0$ arises from the dynamical formation of the halo atmosphere and associated splashback motion in the baryons (e.g. Wetzel & Nagai 2014). In this stacked view the radius of this transition is notably interior to the virial shock, $\sim 0.75 r_{\rm vir}$ as compared to $\sim 1.25 r_{\rm vir}$. Investigating the haloes individually we conclude that this is radial offset is largely a misleading feature arising from the stacking of radially averaged velocity profiles. Instead, the radius of a strong jump in temperature and entropy also closely corresponds to a sudden decrease of inward velocity, as a result of the transfer of kinetic to thermal energy.

• (D) The virial shock seen in a sharp entropy jump from the nearly constant value in the IGM of $\sim 10^{7.7}\,{\rm K\,cm}^2$ to $\sim 10^9\,{\rm K\,cm}^2$ characteristic of the hot gas for haloes of $10^{12}\,{\rm M}_\odot$. The entropy increase occurs over a narrower radial range than the corresponding temperature increase, and at a slightly smaller radius with respect $r_{\rm vir}$. This may be indicative of pre-shock compressive heating, although we caution that this radial difference varies from halo to halo and as shown in the stack. For example, in our subsequent exploration of h0 in Figure 10 we see that there is a close correspondence between the radii of temperature and entropy jumps. After shocking, the entropy slowly declines with radius, following the mean radial profile of the halo.

• (E) The angular momentum distribution is uni-modal and scatters about its mean profile, with no evidence for multiple populations of gas having distinct $j_{\rm gas}$ at any radius.

• (F) The radial velocity depends somewhat on the temperature of the gas, with the hottest gas populating the high positive velocity tail, while cold gas is inflowing. At all temperatures there is a continuous distribution of radial velocities, with an upturn at $\sim 10^6$ K, above which gas has a mean radial velocity consistent with zero, and below which the mean $v_{\rm rad}$ is always negative (see also Joung et al. 2012). The rapidly inflowing hot gas, discussed in (C), is the high velocity tail of the gas distribution at these temperatures and so sub-dominant by mass.

• (G) The usual 'phase-diagram' plotted for cosmological simulations. Cold, low density gas ($n_{\rm gas} \lesssim 10^{-4}\,{\rm cm}^{-3}$) in the IGM (denoted by a star) occupies the lower left corner, the tight relation with $T \propto n^{2/3}$ indicative of adiabatic compression. Shock-heated gas at intermediate densities is the only source for $T > 10^{5.5}$ K gas. At higher densities ($n_{\rm gas} \gtrsim 10^{-3}\,{\rm cm}^{-3}$) strong cooling flows develop at small radii, after which gas approaches the effective temperature floor of $\sim 10^4$ K until it reaches the star formation threshold at $n_{\rm H} = 0.13\,{\rm cm}^{-3}$.

• (H) The heating of inflow, seen here as the dominant temperature for gas at each radial velocity. The handful of strong vertical features are largely an artefact of the stacking. For a given halo, when we restrict this panel to include only gas with $0.2 < r/r_{\rm vir} < 1.0$ we find a clear correlation between deceleration and heating, where gas transitions from cold at -300 km/s to hot by -150 km/s. This is decidedly interior to the virial shock, and outside the galaxy.

• (J) The average radial velocity as a function of entropy, restricted to gas in $0.2 < r/r_{\rm vir} < 1.0$ (not shown) resolves nicely into two distinct populations, where material with $S_{\rm gas} \gtrsim 10^{8.5}\,{\rm K\,cm}^2$ has a mean $v_{\rm rad} = 0$ which is roughly constant. On the other hand, gas with lower entropy than this threshold has a mean $v_{\rm rad} \simeq -150$ km/s, with a gradual trend towards faster inflow with lower entropy.

• (K) Similarly, the average radial velocity as a function of angular momentum, restricted to gas in $0.2 < r/r_{\rm vir} < 1.0$ resolves nicely into two components. Gas with $j \lesssim 10^{4.25}\,{\rm kpc\,km/s}$ has zero mean radial velocity, whereas higher angular momentum gas has $v_{\rm rad} \simeq -v_{\rm vir}$ (this is not shown explicitly in the figure, which includes all gas). The two populations overlap for $10^{4.25} < j_{\rm gas} < 10^{4.5}$. Together with (J) this panel shows the distinct physical properties of the quasi-static and inflowing halo gas.

• (L) Star forming gas has a temperature on the effective equation of state, which is set to a low, constant value to differentiate it from other gas. This results in the constant temperature band at $\simeq 10^{3.5}$ K across this entire row. This gas is restricted to small radii, high densities, low radial velocities, and low angular momenta.

• (M) Gas with high entropy, $S \gtrsim 10^8\,{\rm K\,cm}^2$ has a well defined relation to radius, following the mean halo profile. Below this threshold, if we exclude material in the IGM, gas at any given entropy is essentially distributed throughout the entire halo.

We have seen in several cases how the mean or median radial profiles fail to fully capture the full state and structure of halo gas. Clear examples are the distributions of temperature, entropy, and radial velocity as a function of radius. On the other hand, the distributions of density and angular momentum as a function of radius are comparatively well described by a median and scatter. By measuring average properties within radial bins we implicitly assume that the structure of halo gas is spherically symmetric. Even Figure 8 fails in this regard. For instance, the finite radial thickness of the temperature jump associated with the virial shock could either arise from (i) a spherically symmetric feature of that same thickness, or (ii) the superposition of many thin shocks spread throughout the same radial range, different shock fronts existing at different radii depending on direction. Motivated by the latter possibility, we proceed to investigate and quantify any variation of the structure of halo gas as a function of angle on the sphere.

5 ANGULAR VARIABILITY

As a first step away from radial averages, we consider the properties of gas in a broad radial shell encompassing the regime of interaction between quasi-static material and filamentary inflow. In Figure 9 we plot the distributions of temperature, density, radial velocity, and entropy, for all gas cells within $0.5 r_{\rm vir} < r_{\rm gas} < 1.0 r_{\rm vir}$. In particular, we examine how well the lower resolution runs reproduce the distributions of these quantities found in the highest resolution (L11) runs. In this radial range, we find that the gas of all simulated haloes has broadly similar properties, differing only in the details.

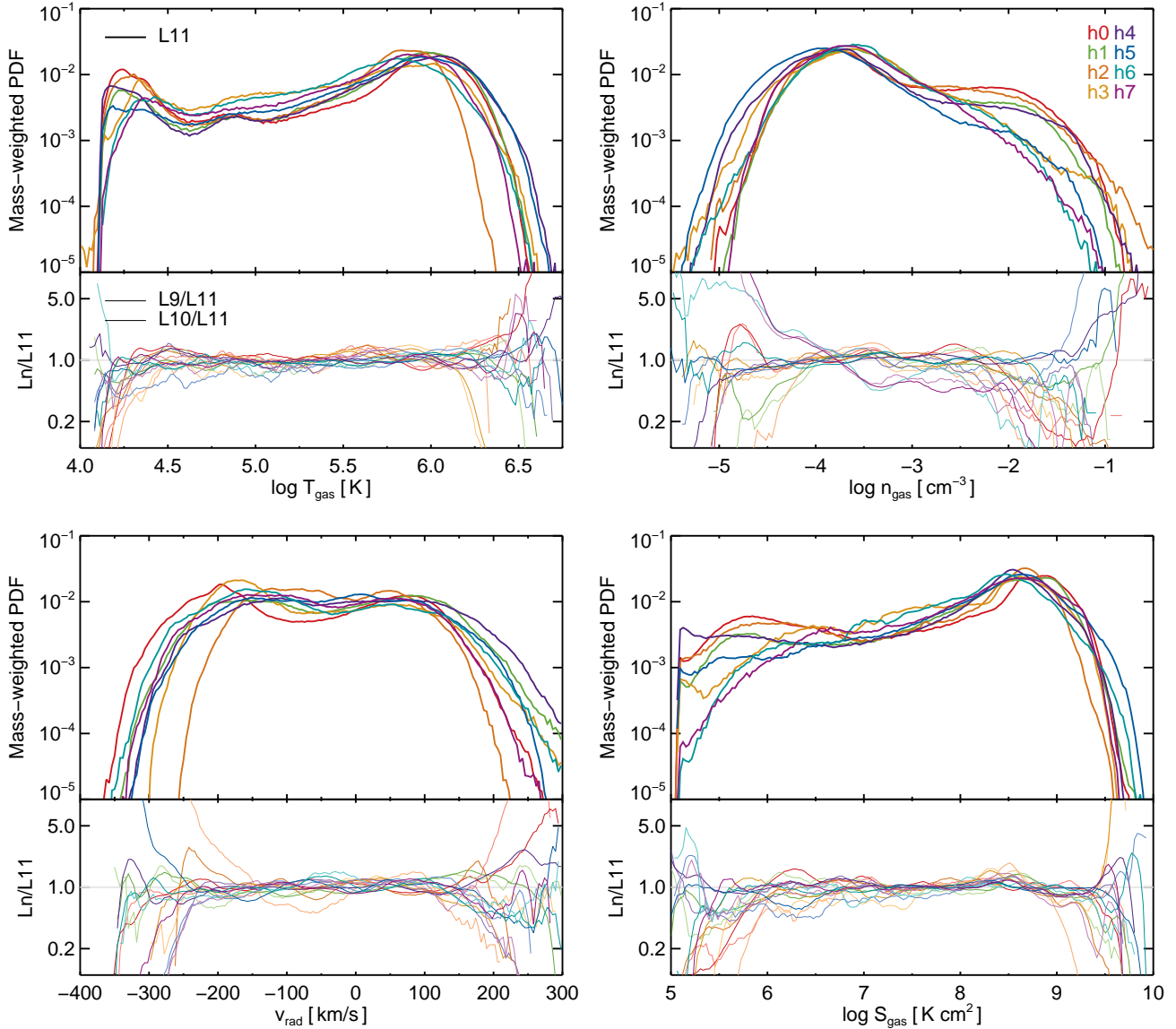The temperature distribution (upper left) shows a

Figure 9. The mass-weighted PDF of instantaneous gas temperature, density, radial velocity, and entropy, restricted to the radial range $0.5r_{\rm vir} < r_{\rm gas} < 1.0r_{\rm vir}$. The upper panel shows all eight haloes at the highest resolution level (L11, different colours), while the subpanels below show the ratio of the two lowest resolution levels to the highest, L9/L11 (thin lines) and L10/L11 (medium lines). The vertical axes of the ratio subpanels are logarithmic from 0.1 to 10. For the most part, the eight haloes show similar structure and their lower resolution counterparts scatter about the L11 distributions (see text for details).

broad peak centred roughly at $T_{\rm vir}$, slowly falling off towards lower temperatures and with a distinct low temperature peak at $\simeq 10^{4.25}$ K. While the fractional amount of gas at each temperature in the L9 and L10 runs can differ throughout this regime by up to a factor of two, depending on halo, the mean ratio of both L9/L11 and L10/L11 is consistent with unity from $10^{4.5}$ K to $10^{6.5}$ K. At the highest temperatures $> 10^{6.5}$ K the lower resolution runs have much larger deviations with respect to L11, but we attribute this primarily to poor sampling of the extreme tail of the distribution due only to a low number of available gas cells. In contrast, the PDF at the low temperature peak is systematically lower in the lower resolution runs. At $\simeq 10^{4.25}$ K where

there are still a large number of gas cells, the mean across all eight haloes is L9/L11 $\simeq 0.5$ and L10/L11 $\simeq 0.8$, indicating that there is a smaller fraction of the total gas mass at these temperatures at lower numerical resolution. Note that 10^4 K is effectively the temperature floor due to cooling in these simulations, and the mean $T_{\rm IGM}$ at redshift two is just above this value.

Gas density shows an even larger variation on a halo to halo basis – some have a strong second peak at higher densities, while this feature is largely absent for the less relaxed haloes. The ratio with respect to the lower resolution runs is consistent with unity for $\log n_{\rm gas} < -2.5\,{\rm cm}^{-3}$. Between this value and the star formation threshold of $\simeq 10^{-1.0}\,{\rm cm}^{-3}$,

there is a decrease, at lower resolutions, in the fractional amount of gas at these densities. In this range, the mean ratio across all eight haloes is L9/L11 $\simeq 0.4$ and L10/L11 $\simeq 0.6$. As with temperature, we see that the density PDFs can disagree between resolutions by as much as a factor of ten, but only in the tails when the magnitude drops to low values of $\leqslant 10^{-4}$. The disagreement is similar with radial velocity, where the mean Ln/L11 ratios are consistent with unity for all values away from the extremes.

The distribution of v_{rad} itself is comprised of two broad components, roughly centred about zero, the positive and negative peaks indicative of outflow and inflow, respectively. The primary driver of inter-halo variation – for example, that h0 has smaller minimum and maximum velocities – appears to be differences in assembly history, particularly a recent merger with another massive halo, or lack thereof. We explore this further in the following section. Finally, gas entropy behaves similarly to temperature, where we find that low entropy gas is strongly sub-dominant by mass with respect to the high entropy hot halo material. The largest variation between haloes occurs for $\log S_{\mathrm{gas}} < 10^6 \,\mathrm{K\,cm^2}$, down to the floor at $\simeq 10^5 \,\mathrm{K\,cm^2}$. The halo-average PDF at L9 and L10 reveals a smaller fraction of gas at these lowest entropies when compared to the L11 run.

In general, we conclude that for any given halo, large variations between the three resolution levels can be seen, with deviations up to a factor of ten in the fractional amount of gas at a particular temperature, density, radial velocity, or entropy. These deviations occur mostly in the tails of the distributions which are poorly sampled at the lower resolution levels. Furthermore, the timing differences present in any single comparison likely influence some of the largest outliers. With respect to the average behaviour across all eight haloes, we find that the lower resolution runs have less low temperature, high density, and low entropy gas. By mass fraction with respect to the total gas mass in this radial range, the magnitude of the effect is ~ 2 (~ 1.5) for L9 (L10), although it is unclear if this gas population is necessarily converged for these haloes at L11.

5.1 Structure Along Radial Sightlines

To proceed, we consider sightlines originating outwards from the halo centre in different directions, which will have different radial structure. If the hot halo gas was triaxial, for example, we could anticipate that the radius of a strong virial shock would differ along its major and minor axes. We therefore measure the angular variability of the thermal and dynamical structure of the halo by casting many such sightlines from the centre of each halo. Along each of these 'radial rays' we sample the continuous fields of gas temperature, radial velocity, entropy, density, and angular momentum in fixed steps of Δr. Using this ensemble of rays we can then quantify the structure of halo gas without binning in spherically symmetric radial shells.

Ray directions are set using the HEALPIX discretisation of the sphere (Górski et al. 2005) into equal area pixels, which implies equal angular spacing of rays at all refinement levels. The total number of radial rays is $N_{\mathrm{ray}} = 12N_{\mathrm{side}}^2$, corresponding to an area subtended by each ray equal to $\Omega_{\mathrm{ray}} = 4\pi/12N_{\mathrm{side}}^2$ sr, or $\theta_{\mathrm{ray}} = (180^2/3\pi N_{\mathrm{side}}^2)^{1/2}$ deg. The sampling in the radial direction is linear and controlled

by the parameter N_{rad} such that $\Delta r/r_{\mathrm{vir}} = 2.0/N_{\mathrm{rad}}$. Our fiducial parameters of $N_{\mathrm{rad}} = 400$, $N_{\mathrm{side}} = 64$ result in a sampling of $\Delta r \simeq 0.5\,\mathrm{kpc}$ and $\Delta\theta = 1\,\mathrm{deg}$. At each point, mean gas properties are estimated with a tophat kernel with adaptive size equal to the radius of the sphere enclosing the $N_{\mathrm{ngb}} = 20$ nearest gas neighbours.[5]

In Figure 10 we show a snapshot of the combined radial and angular structure of a single halo (h0L11) at $z = 2$. The twelve demarcated intervals along the y-axis denote the twelve base pixels of the HEALPIX discretisation. Within each base pixel the nested ordering scheme uses a hierarchical quad-tree to preserve adjacency, and the four subintervals delineate the top nodes of each such quad-tree, implying that structure seen in the vertical direction is spatially coherent within these major and minor intervals. We note that there is no mass weighting or, for that matter, any indication of the mass distribution within each of the five panels, since the sampling points are smoothly distributed throughout the volume regardless of the underlying gas cell distribution.

Focusing first on the temperature structure we clearly see a boundary separating the cold, intergalactic medium from hot, virialised gas. At this halo mass scale, the temperature increases by roughly two orders of magnitude, from $\simeq 10^4\,\mathrm{K}$ to $\simeq 10^6\,\mathrm{K}$ (dark blue to yellow/orange). In some directions this heating is coherent and occurs at essentially uniform radius (for example, 9-10, marked 'A'), demarcating a clear 'virialization boundary'. However, across all sightlines we also observe a temperature jump of similar magnitude anywhere from $1.0 < r/r_{\mathrm{vir}} < 1.5$, and smaller jumps can occur out to twice the virial radius. Even so, from Figure 3 we know that this halo is one of the most spherically symmetric, with a noticeable transition in the state of gas just outside the virial radius. In directions where the gas temperature is warm and exceeds $\sim 10^5\,\mathrm{K}$ out to twice r_{vir}, we find a correspondence to a baryonic overdensity, with respect to mean at that distance. This is indicative of large-scale gas filaments and the heating associated with their earlier collapse.

Interestingly, in directions where gas coherently penetrates to radii smaller than the virial radius and remains cold (e.g. B), this same correspondence to overdensities at larger distance remains. Qualitatively, the existence of an inflowing gas filament arising from the cosmic web suppresses a strong shock at the virialization boundary. This can arise from previous heating from filament formation outside of the halo, which increases the gas temperature to an intermediate state between T_{IGM} and T_{vir}. There can nonetheless be a (smaller) temperature jump around the mean virialization boundary (C), although this is not always true and gas can gradually heat seemingly all the way to the peak of the halo temperature profile just exterior to the disc region (e.g. D). Alternatively, this shock suppression can also arise from a delay of strong heating to deeper within the halo, in which

---

[5] This is close to the mean number of natural neighbours (or cell faces) of the evolved Voronoi mesh in a cosmological simulation (Vogelsberger et al. 2012). Therefore the spatial scale of this effective smoothing is approximately matched to the scale of the stencil used in gradient estimation for linear reconstruction of fluid quantities in the MUSCL-Hancock scheme of AREPO (Springel 2010).
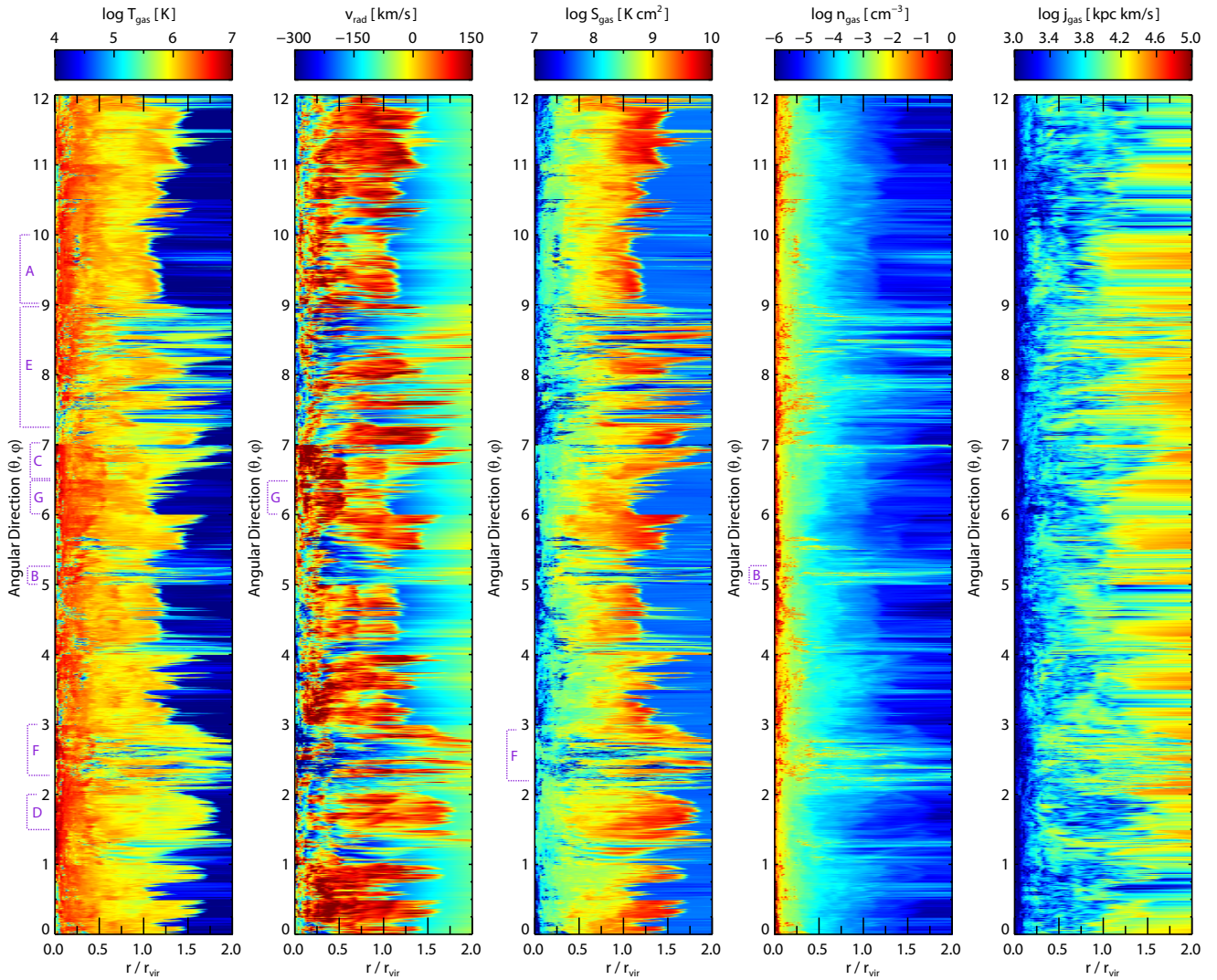
Figure 10. The angular variability of gas temperature, radial velocity, entropy, density, and angular momentum at a given radius. Each pixel along the vertical direction represents a single radial ray, which are equally spaced in angular separation. The radial variability of the virial shock is evident in the shifting boundary between dark blue and yellow/orange in the left panel. Penetration of low temperature gas to radii smaller than $r_{\rm vir}$ correlates with higher inflow velocities, lower entropy, and higher density, often extending out into the IGM at $r \geqslant 2r_{\rm vir}$. In this figure we include only a single halo, h0L11, with $N_{\rm side} = 16$, $N_{\rm rad} = 100$. All substructures other than the primary have been excised, thereby excluding satellites.

case there is less preheating evident at large distances. The radius of the strongest temperature jump then decreases, typically to $0.25r_{\rm vir} < r < 0.75r_{\rm vir}$ as in much of (E). There are essentially no sightlines along which the gas does not experience heating above $T_{\rm IGM}$ at some radius. Since the velocity field, and so the streamlines of accreting gas, are not purely radial, this does not preclude the possibility that gas could avoid heating along its actual dynamical path. Such a trajectory would be curved in these panels. In some cases (F) we can largely rule out this behaviour, since over a large coherent solid angle no cold gas at $r < 0.5r_{\rm vir}$ is directly connected to cold gas at larger radii. In general, however, the analysis based on radial rays is limited in this respect.

As with density, we also see a strong correlation between temperature and both entropy and radial velocity. Strong temperature jumps just outside the virial radius are

also evident as sharp transitions from the gradually increasing (negative) IGM inflow velocity, through equilibrium, to a generally (positive) outflow speed indicative of the virialised halo gas. In some directions (G) multiple components are clearly visible, where an inner halo is comprised of hotter, denser, and more rapidly expanding gas which has more recently bounced back under its own thermal pressure. Similarly, the entropy of the low-density IGM undergoes a sharp increase before declining towards the halo centre. On a sightline by sightline basis the radius of the entropy jump is nearly equal to that of the temperature and radial velocity jumps. Finally, the angular momentum of the gas is clearly the least affected by the virialization boundary. As the velocity field becomes increasingly complex towards smaller radii, the non-radial component contributing to the angular

momentum does not have a clear correlation with any of the other local gas properties.

5.2 Different Gas Heating Regimes

To understand the properties and the importance of sightlines exhibiting different radial behaviours, we would like to identify a few characteristic types. We separate rays into a small number of disjoint sets in Figure 11, each group ideally having a distinct radial behaviour. By visual classification we identify four such groups, which together encompass the majority of sightlines. In particular, we split rays into 'distant shock', 'closer shock', 'gradual heating', and 'low entropy' types, each of which is based on a quantitative selection applied across some radial range. Specifically, for the 'distant shock' type we require all of

- $\max(\mathrm{d}T/\mathrm{d}r|_{0.2<r<2.0}) > 0.25$
- $1.5 < r_{\max(\mathrm{d}T/\mathrm{d}r)} < 2.0$
- $\min(T_{\mathrm{gas}}|_{0.2<r<1.4}) > 2 \times 10^5 \,\mathrm{K}$

where $\mathrm{d}T/\mathrm{d}r$ denotes the derivative of gas temperature with respect to radius, in units of $(\log \mathrm{K})/(0.1\,r_{\mathrm{vir}})$, $r_{\max(Q)}$ indicates the radius where the quantity Q reaches its maximum value, and $Q|_{r_1<r<r_2}$ indicates that a quantity Q is constrained only within the radial range between r_1 and r_2. For the 'closer shock' type we require

- $\max(\mathrm{d}T/\mathrm{d}r|_{0.2<r<2.0}) > 0.25$
- $0.8 < r_{\max(\mathrm{d}T/\mathrm{d}r)} < 1.5$
- $\min(T_{\mathrm{gas}}|_{0.2<r<0.7}) > 3 \times 10^5 \,\mathrm{K}.$

That is, both must exhibit a strong temperature jump at either large or intermediate radii, while excluding rays which subsequently drop to low temperature at smaller radii – an artefact of intersecting non-radial cold debris, as we subsequently discuss. Of the remaining rays not meeting the prior two conditions, we further require rays of a 'gradual heating' type to satisfy

- $\max(\mathrm{d}T/\mathrm{d}r|_{0.2<r<2.0}) < 0.8$
- $\min(T_{\mathrm{gas}}|_{0.2<r<0.75}) > 3 \times 10^5 \,\mathrm{K}.$

Finally, the 'low entropy' type requires of any remaining rays

- $\max(S_{\mathrm{gas}}|_{0.2<r<2.0}) < 8 \times 10^8 \,\mathrm{K\,cm^2}.$

In Figure 11 we show all four groupings as separate panels (for halo h0L9). The temperature is plotted as a function of radius, while colour indicates gas entropy. A single prototypical ray is included as a thick line, while all rays belonging to that type are shown underneath as thin lines. The mean radial velocity profile of all rays of that type, locally averaged in radius, is denoted by the series of numbers shown in each panel, in units of km/s (negative denoting inflow). The top inset above each panel plots the temperature derivative $\mathrm{d}T/\mathrm{d}r$, positive denoting increasing temperature with decreasing radius, for the prototypical ray (thick) and five other random sightlines of that type (thin).

We briefly describe the behaviour of each type. Sightlines experiencing a 'distant shock' undergo a jump in temperature from $\simeq 10^4\,\mathrm{K}$ to $\simeq 10^6\,\mathrm{K}$ over a radial range of $\sim 0.1 r_{\mathrm{vir}}$ (although, as in the example, multiple jumps can exist and be spread over a larger radial range). At this same radius the entropy also increases by approximately two orders of magnitude, from $\simeq 10^{7.5}\,\mathrm{K\,cm^2}$ to $\simeq 10^{9.5}\,\mathrm{K\,cm^2}$. The

Table 3. The percentage of radial rays of each of the four types: 'distant shock', 'closer shock', 'gradual heating', and 'low entropy'. The mean fraction across all eight haloes is calculated separately for each resolution level. Since rays cover equal angular area, each fraction corresponds to the geometrical percentage of the sphere occupied by sightlines satisfying each criterion. The errors represent the standard deviation among the eight haloes.

type	L9	L10	L11
distant shock	23.6 ± 4.8	17.3 ± 4.9	12.5 ± 6.1
closer shock	22.5 ± 15.9	27.2 ± 14.0	30.4 ± 15.2
gradual heating	28.0 ± 15.2	14.5 ± 7.9	6.2 ± 3.9
low entropy	7.1 ± 2.7	7.5 ± 3.8	5.4 ± 2.9

rapid inflow velocity decreases, reaching its maximum (positive) value near the radius of maximum temperature. Towards smaller radii, the ray temperature then follows the steadily increasing mean temperature profile of the halo, until reaching the centre. The 'closer shock' sightlines have the same behaviour – the radial distinction between close and distant shocks is arbitrary. In either case, the temperature profile can be non-monotonic if the shock occurs at sufficiently large radius, such that the shock temperature is greater than the local mean $T_{\mathrm{gas}}(r)$, and the gas can subsequently cool. Heating can be associated with one or multiple shocks (e.g. two, in the case of the prototypical example shown in the upper left panel). The maximum derivatives of temperature and entropy are $\simeq 2.0$ (in log) per $0.1\,r_{\mathrm{vir}}$, although the typical maximum along any given ray is roughly half as large.

The 'gradual heating' sightlines generally reach the same maximum temperature (in the inner halo) and entropy (near the virialization boundary), but do so without any sudden jumps. Here the inflow velocity is roughly constant and always negative, never approaching a quasi-static state, increasing towards smaller radii and with a mean of approximately -75 km/s. The 'low entropy' rays are selected to have a maximum entropy of less than $8 \times 10^8\,\mathrm{K\,cm^2}$, although the exact value is arbitrary. In this case, the inflow velocity is always strongly negative, peaking in the inner halo, with a mean of approximately -135 km/s. The vast majority of these rays still reach high temperature, but at $\lesssim 0.25 r_{\mathrm{vir}}$ and possibly not until the disk-halo interface. At $r > 0.5 r_{\mathrm{vir}}$ we see that 'low entropy' sightlines also have systematically lower temperatures and higher inflow velocities than the other three types.

In Table 3 we include the fraction of each of these four ray types, calculated as the mean over all eight haloes. Although the balance between the two shock types shifts with resolution, the total ray fraction experiencing a strong shock remains at $\simeq 45\%$, with the temperature jumps moving somewhat inwards. The gradual heating fraction drops sharply at higher resolution levels, either because fluctuations become better resolved, or because the adopted cut on the temperature derivative is slightly too restrictive. The low entropy ray fraction remains fairly converged at $\simeq 6\%$.

We have verified that these values, and all the other quantitative results related to the radial rays, are well converged with the numerical parameters $N_{\mathrm{rad}} = 400$, $N_{\mathrm{side}} = 64$. Given our selections, approximately $\simeq 15\%$ of the sight-
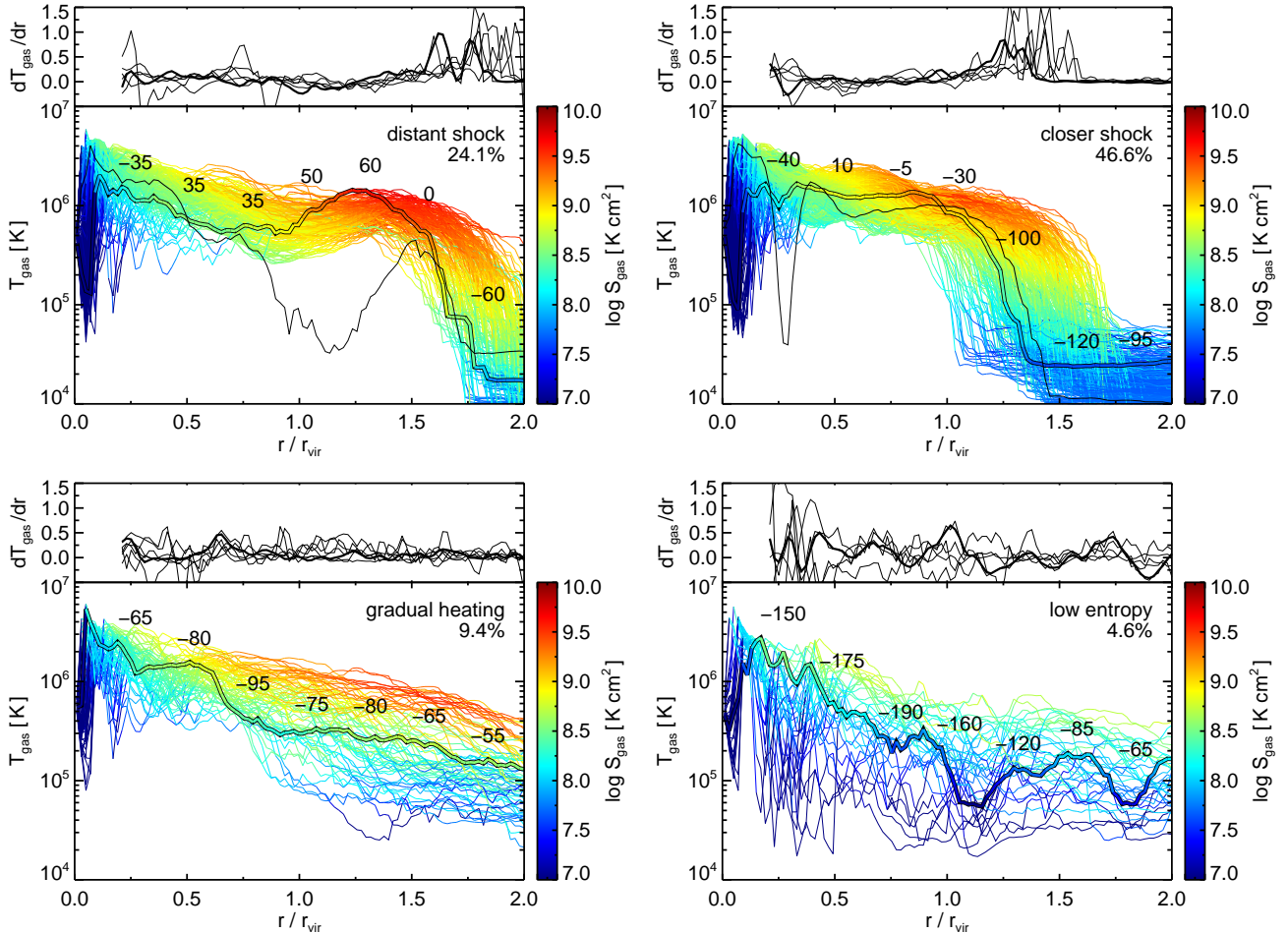
Figure 11. The temperature profiles of individual radial rays (four main panels), with colour indicating gas entropy. Each of the four panels includes a disjoint subset of the entire ray set, where the selection for each was chosen by visual inspection in order to find four types of sightlines, each with similar radial properties, which together cover the majority of behaviours. In each panel, all rays are shown as thin lines, while a single prototypical example is shown as a thick coloured line. The mean radial velocity profile for each ray type is indicated by the series of numbers (in units of km/s, negative denoting inflow). The smaller top insets show the derivative of gas temperature with respect to radius, in units of $(\log K)/(0.1\, r_{\rm vir})$. The percentage in each panel indicates the fraction of all rays satisfying the criteria, for this particular halo. Given our selections, some sightlines are excluded from all four types. The vast majority of these rays either fall just outside a selection, or experience a significant temperature dip within the halo, which is a signature of satellite debris or intersection with non-radial filamentary inflows. Two such examples are shown as thin black lines in the upper two panels. In this figure we include only one halo, h0L9, with $N_{\rm side} = 8$ and $N_{\rm rad} = 100$ for visual clarity.

lines remain excluded from all four types at L9, although this increases to $\simeq 45\%$ at L11. The vast majority of these excluded rays either (i) fall just outside a selection, or (ii) experience a significant temperature dip within the halo. By definition they do not satisfy the 'gradual heating' or 'low entropy' conditions. Two such examples are shown as thin black lines in the upper two panels. We find that the narrow dips are typically a signature of intersecting satellite debris or satellite outskirts, which were not calculated as locally gravitationally bound and so were not excised. Gas cells of this type fill a larger fraction of the halo volume at higher resolution, leading to the increased percentage of rays excluded from all four types. Broader dips are typically intersections with large filamentary inflows which are not aligned in the radial direction. This exposes the main caveat of the above analysis – namely, that gas inflow with a tangential

velocity component need not evolve according to the temperature, entropy, or velocity structure of any particular radial ray.

5.3 Quantifying The Asphericity of Temperature

In order to quantify the instantaneous halo temperature structure, we calculate differential histograms of radii satisfying a given criterion in Figure 12 (top panel). First, solid lines show the distribution of the maximum radius, for each radial ray, where the temperature exceeds some fraction of $T_{\rm vir}$ (different colours). To avoid washing out features by stacking, we include only one halo (h0L11). We see that for the three lowest temperature cuts, $(0.1 - 0.5) \times T_{\rm vir}$, the $r_{\rm max}$ values all show a strong peak at $\simeq 1.2\, r_{\rm vir}$, indicative
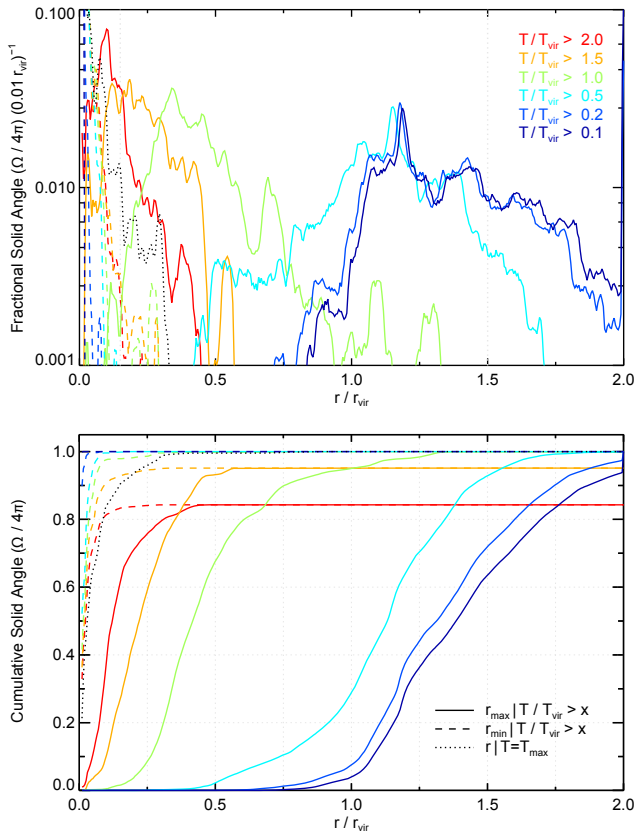
Figure 12. (Top) The histogram of radii satisfying three different types of criteria (different linestyles), computed separately for each radial ray. Since each subtends equal angle, this histogram is equal to the fractional solid angle of the whole sphere covered by rays satisfying each criteria, as a (differential) function of radius. The criteria are: (i) the maximum radius at which the temperature along the ray exceeds some fraction of $T_{\rm vir}$, (ii) likewise, but the minimum radius, and (iii) the radius at which each ray reaches its maximum temperature. For the first two conditions, we consider six different temperature thresholds (from blue to red). In this figure we include only one halo at the high resolution level, h0L11, with $N_{\rm side} = 64$ and $N_{\rm rad} = 400$. (Bottom) As in the upper panel, but here as a cumulative function of radius.

of the virialization boundary. The distributions are broad, however. In the case of $T/T_{\rm vir} > 0.5$ the spread of maximum radii is roughly symmetric, extending from $0.5r_{\rm vir}$ out to $1.6r_{\rm vir}$. That is, although the majority of sightlines first exceed $0.5T_{\rm vir}$ at a well-defined surface sitting at $1.2r_{\rm vir}$, a non-negligible fraction first exceed this temperature already by $1.6r_{\rm vir}$, and an even larger fraction cross this threshold inside the virial radius, between $0.5 - 0.75r_{\rm vir}$.

The three higher temperature thresholds (green, orange, red) reflect the increasing mean radial temperature profile of the halo. The virial temperature is typically reached at $\simeq 0.5\,r_{\rm vir}$, while gas reaches twice $T_{\rm vir}$ just prior to the galaxy at $\simeq 0.1\,r_{\rm vir}$. The dashed lines show the minimum radius where each temperature threshold is reached. They are uniformly peaked at the halo centre. Finally, the dotted line plots the distribution of the radius where each ray reaches its maximum temperature, which are also peaked in the halo centre. One of our principal goals is to

identify gas shocking at the halo-IGM transition. We see that the peak of the radial distribution, for rays satisfying $r_{\rm max}(T/T_{\rm vir} > \{0.5, 0.2\})$, measures the most dominant radius for this transition. With respect to halo to halo variability, we find that the shapes and overall widths of each $r_{\rm max}$ distribution can vary substantially. For instance, h0 has a strong peak which is both the narrowest in radius and the most covering in angular fraction. Yet, it also has a prominent secondary peak of roughly half the geometrical importance at larger radius, $\Delta r \simeq 0.2r/r_{\rm vir}$ further from the halo centre. Even more extreme, h3 has two peaks of equal strength spaced $\Delta r \simeq 0.5r/r_{\rm vir}$ apart. Multiple radial peaks are a common occurrence.

The widths of the distributions also encode a measure of the spherical symmetry of any strong heating. Here it is useful to look at the cumulative histograms of radii satisfying these same temperature criteria, as shown in the bottom panel of Figure 12. The slope of this CDF indicates angular uniformity – presence of a Heaviside step function would indicate perfect spherical symmetry, while slopes approaching zero would indicate that the temperature transition takes place, depending on sightline, over widely disparate radii. The fact that several temperature thresholds plateau below unity indicate that only $\simeq 85\%$ of rays reach $T > 2.0T_{\rm vir}$ (red line) and $\simeq 95\%$ of rays reach $T > 1.5T_{\rm vir}$ (orange line), while all other temperature thresholds are exceeded along all sightlines. Any value for the cumulative solid angle can provide a good way to quantify the location of the mean virialization boundary. For instance, the radius by which 2π sr are covered by rays with maximum temperature exceeding half of $T_{\rm vir}$ is $\simeq 1.1r_{\rm vir}$.

We conclude with a visual impression of the three-dimensional temperature structure in and around a single halo (h0L11) in Figure 13. A ray-traced volume rendering highlights five iso-temperature surfaces using the same blue-red colortable and physical bounds of $4.4 < \log T_{\rm gas}$ [K] < 6.3 as in the temperature projections of Figure 3. It is sampled with a transfer function comprised of four narrow alpha-channel gaussians at $\log T_{\rm gas}$ [K] $= \{4.5, 5.0, 5.5, 6.0\}$ with widths of $\sigma = \{6, 6, 3, 3\} \times 10^{-3}$ in log K. The scale of the image is $5.5\,r_{\rm vir}$ in both height and depth, as in the zoomed out panels of Figure 5. The dark blue surface straddles the mean $T_{\rm IGM}$ at $\simeq 2r_{\rm vir}$ and reveals a morphology at overdensities just below cosmic web filaments. The light blue surface at 10^5 K clearly outlines the structure of Mpc-scale, large-scale filaments, while the yellow surface at $10^{5.5}$ K is restricted to the interior of warmer filaments. Both of these two iso-temperatures surfaces are closed. Further, they enclose the virialised halo itself – we can see how the filamentary shape of the 10^5 K surface at $r > 2r_{\rm vir}$ transitions smoothly into a quasi-spherical shape by opening up, wrapping around and encompassing the higher temperature shells. The mean radius of the $10^{5.5}$ K surface is $\simeq 1.0\,r_{\rm vir}$, while that of the 10^6 K surface is $\simeq 0.5\,r_{\rm vir}$. The intersection of radial sight-lines cast outwards in different directions with this complex temperature structure in and around the $10^{12}\,{\rm M}_\odot$ halo gives rise to the four distinct ray types described earlier.
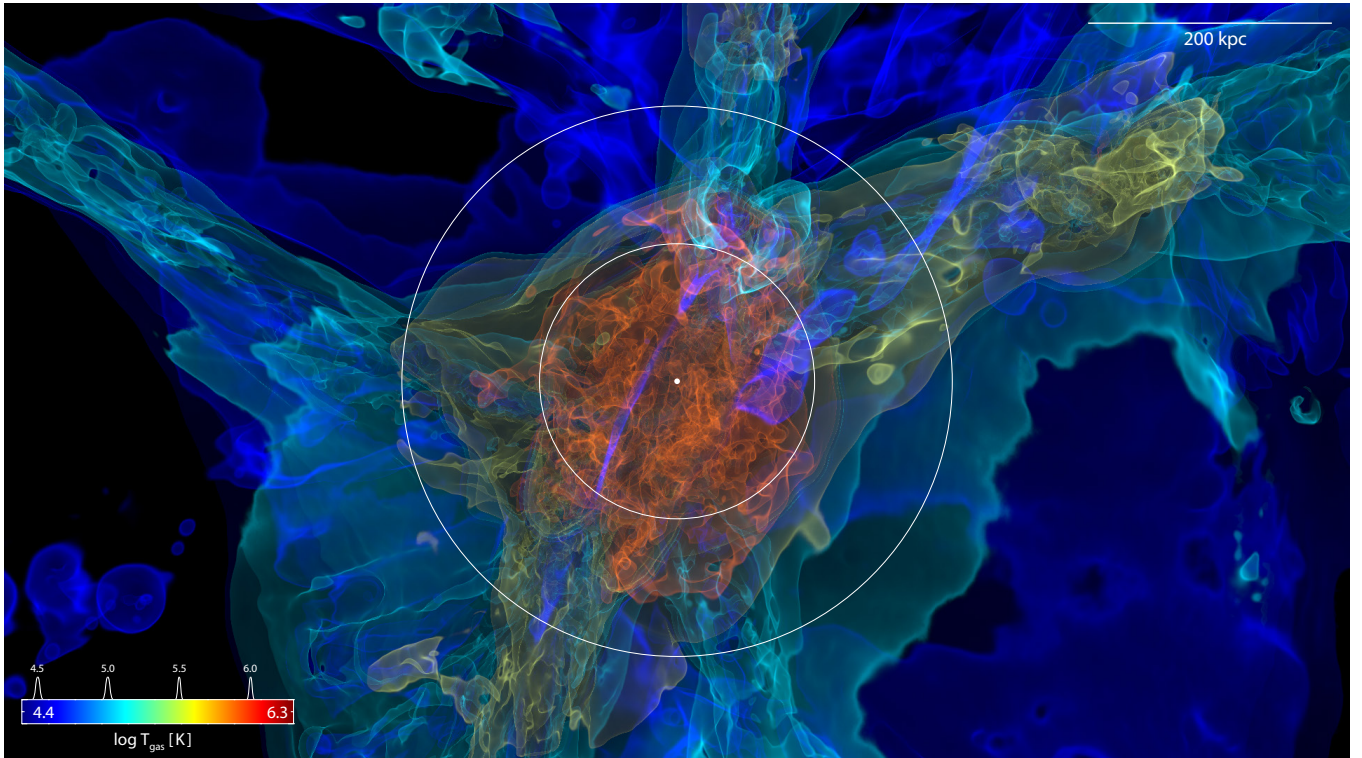
Figure 13. A volume rendering of the three-dimensional temperature structure around a single halo (h0L11) at $z = 2$. We use an orthographic projection with depth and height equal to $5.5\,r_{\rm vir}$ ($\simeq 620\,{\rm kpc}$), as in the zoomed out panels of Figure 5. The colortable and 4-gaussian transfer function are shown. A front-to-back ray tracing method is used, with no scattering and no absorption. Along each ray we sample with a constant step-size of 0.25 kpc. The temperature at each sample point is calculated using the standard cubic-spline SPH kernel interpolant with adaptive smoothing length h over the $N = 200$ nearest neighbours (the representation of the gas in terms of a Voronoi tessellation is not used). The white dot marks the halo centre, and the white circles denote one and two times the virial radius.

6   DISCUSSION

6.1   Observational Points

We have deferred a direct comparison against observations of the gas content of haloes to future work. Such a comparison deserves a careful treatment of the various steps required to make robust synthetic (or 'mock') observations from the simulations, for both hydrogen (e.g. Faucher-Giguère et al. 2011; Faucher-Giguere et al. 2014; Fumagalli et al. 2014; Bird et al. 2014) as well as metal signatures (e.g. Shen et al. 2013; Hummels et al. 2013; Ford et al. 2014; Suresh et al. 2015). As motivation and in preparation for the next work in this series, there are a number of insightful observations of the gas in and around haloes with masses of $\sim 10^{12}\,{\rm M_\odot}$ at $z \sim 2$ which prompt mention here.

Observations have studied the incidence and kinematics of HI absorption around haloes of this mass (e.g. the Lyman-break galaxies of Rudie et al. 2012, 2013). They found, for instance, a covering fraction for Lyman-limit systems within the virial radius of $\sim 30\%$. The hydrogen and metal content around lower mass damped Lyman-alpha systems (DLAs, $\sim 10^{11}\,{\rm M_\odot}$ haloes) at this redshift is roughly consistent with their $10^{12}\,{\rm M_\odot}$ counterparts (Rubin et al. 2014), where the covering fractions within $100\,{\rm kpc}$ of strong Si II absorption was found to be $\sim 20\%$, versus $\sim 60\%$ for strong C IV.

Around more massive 'quasar hosts' of $\sim 10^{12.5}\,{\rm M_\odot}$ the covering fractions of neutral hydrogen are larger (Prochaska

et al. 2013). On the scale of the virial radius in such haloes the covering fractions of cold metal ions (e.g. C II and C IV in Prochaska et al. 2014) are even higher and may approach unity. The presence of cold gas at large radii (Turner et al. 2014b) is a result which, in general, current hydrodynamical simulations have significant difficulty reproducing. On the other hand, hot gas as often probed by O VI at these redshifts (Turner et al. 2014a) is more readily reproduced given sufficiently energetic outflows (Ford et al. 2013; Suresh et al. 2015). In some cases there is strong evidence that the observed absorption results from high velocity galactic outflows (Crighton et al. 2015). Other observations imply that slower inflowing structures with a high degree of kinematic coherence are more likely (Rubin et al. 2014). In general, it is unclear if the cold gas seen in the haloes surrounding galaxies is *always* the consequence of one of (i) feedback-driven outflows (e.g. Marinacci et al. 2014b) or (ii) cosmological inflow, or if this depends on the halo mass under investigation. Either way, it is currently difficult, from the theoretical perspective, to explain how this cold gas is generated, distributed, and either maintained or replenished in the halo.

6.2   The Resolution Issue

Observations have also placed constraints on the physical size of the systems which give rise to metal absorption in gaseous haloes. Simcoe et al. (2006) estimated absorbers

sizes around $z \sim 2.3$ galaxies ranging from the sub-parsec to the kiloparsec. This is consistent with the transverse scales of C IV absorbers derived in Rauch et al. (2001) from multi-sightline analysis of lensed QSOs at sub-kpc scales (see also Petitjean et al. 2000, based on Mg II). Based on photo-ionization modelling of C IV absorbers at similar redshifts, Schaye et al. (2007) derived typical densities of $n_{\rm H} \sim 10^{-3.5} \, {\rm cm}^{-3}$ with sizes of $\sim 100 \, {\rm pc}$. Similarly, Crighton et al. (2015) observe metal absorption lines arising near a $z \simeq 2.5$ galaxy and derive a $(< 100 - 500) \, {\rm pc}$ size constraint, which they argue is a ubiquitous size-scale for all low-ion halo gas in the circumgalactic environments of both low and high redshift galaxies. Pieri et al. (2014) conclude that a typical low-ionization absorber associated with the CGM of strong Lyman-alpha forest systems at $z \sim 2.5$ is $\sim 30 \, {\rm pc}$ in size. Furthermore, the gas giving rise to various absorption lines may also have unexpected geometries with little resemblance to spherical clouds (Churchill et al. 2014).

Obtaining $\sim 100 \, {\rm pc}$ hydrodynamic resolution at the virial radius by simply running higher resolution simulations of isolated haloes will be prohibitively expensive. Following the observed scaling of the gas resolution in the halo, we would obtain a mean $r_{\rm cell} \simeq 0.1 \, {\rm kpc}$ physical at $z = 2$ with a L14-class simulation. That is, gas mass resolution approaching $30 \, {\rm M}_\odot$, requiring $\gtrsim 10^{10}$ gas cells in a $10^{12} \, {\rm M}_\odot$ halo. This is not a realistic goal for the near future. Even given such a simulation, the minimum size of resolved clouds would be a few times larger than the size of individual resolution elements.

On the other hand, numerical methods may enable novel ways to focus resolution within the halo regime. If we can avoid clustering the computational effort in the densest regions of space – within galaxies themselves – much higher spatial resolutions can be achieved in lower density media. In AMR simulations, the refinement criterion can be chosen as desired, on the gradient of the neutral hydrogen fraction for instance (Rosdahl & Blaizot 2012), or with a progressively refined uniform Eulerian grid which is volume filling (Miniati 2014). In our moving mesh simulations, we can enforce a target gas cell mass criterion of any type through adaptive refinement and de-refinement of Voronoi cells. In future work we will explore this possibility as a solution to the resolution issue, in addition to quantifying the rates and modes of accretion using the tracer particle information.

7 CONCLUSIONS

In this first paper of the series we present a suite of high-resolution cosmological hydrodynamic zoom-in simulations targeted at understanding the properties of halo gas and cosmological accretion in $\sim 10^{12} \, {\rm M}_\odot$ haloes at $z = 2$. Using the moving-mesh code AREPO we simulate each of eight haloes at three levels of increasing resolution, reaching a mean baryonic mass of $\sim 10{,}000$ solar masses. We study the thermal and dynamical state of halo gas within $2 \, r_{\rm vir}$ and in particular quantify density, temperature, entropy, angular momentum, and radial velocity in terms of their mean radial profiles and, more interestingly, in terms of their variation along radial sightlines in different directions.

In this mass regime, haloes typically reside at the intersection of one or more 'cosmic web' filaments arising from large-scale structure. The result is a significant amount of filamentary inflow across the virial radius.

• Investigating the interaction of this inflow and the quasi-static hot halo atmosphere, we find that stream morphologies become continuously more complex with better numerical resolution. In general, single coherent flows tend to resolve into multiple, narrower streams while producing density and temperature structure at smaller spatial scales. However, we point out that even at our highest resolution – comparable to the best zoom-in simulations that currently exist for haloes of this mass – the gas-dynamics in the circumgalactic regime are poorly resolved in comparison to within galaxies themselves.

• In general, the mean radial profiles of gas properties are well captured at our lowest resolution – equivalent to that currently available in full cosmological volume simulations. However, gas which is stripped from infalling satellites, or which forms as the result of a strong tidal interaction, is less well converged, and populates the halo with additional high density gas in our highest resolution runs.

• Although average radial profiles are well converged, their direct interpretation can be misleading. Within the halo itself, $0.2 < r/r_{\rm vir} < 1.0$, there are clearly multiple gas components overlapping in radius and corresponding to quasi-static versus inflowing material. For example, although the mean radial velocity within the halo is near zero (equilibrium), this is not true for the majority of gas, which is actually either inflowing or outflowing.

• Examining the thermal and dynamical state of gas within $2 \, r_{\rm vir}$, we clearly identify the existence of a strong virial shock. This 'virialization boundary' typically resides at $(1.25 - 1.5) \times r_{\rm vir}$ and is evident as a sharp increase in gas temperature, entropy, density, and a decrease in inwards radial velocity. Collimated inflows which remain cold past the virial radius experience significant heating, typically at $\sim 0.5 r_{\rm vir}$, from $\lesssim 10^{4.5} \, {\rm K}$ to $\gtrsim 10^6 \, {\rm K}$.

• Although the mean radius of a strong virial shock may be $\simeq 1.25 \, r_{\rm vir}$, our sightline analysis allows us to identify, in each halo, many radially-sharp virial shocks, each at some radius between $1.0 \, r_{\rm vir}$ and $1.5 \, r_{\rm vir}$, depending on angle on the virial sphere.

• Investigating the process of gas virialization, we identify different mechanisms responsible for the heating of gas in the circumgalactic regime. In addition to a single strong virial shock at $\lesssim r_{\rm vir}$, we find that gas can shock at much larger radii, $\lesssim 2 \, r_{\rm vir}$, particularly in systems where the hot halo is far from equilibrium and can extend to these distances due to the dynamical response of a recent major merger. We also see that gas can heat gradually, with temperature increasing slowly from its characteristic IGM value until reaching the mean halo temperature profile. Finally, we identify the existence of radial sightlines along which gas entropy remains always below the level characteristic of the hot halo. Even in this case, however, gas cannot avoid heating to $\sim T_{\rm vir}$ in the inner halo, $\sim 0.2 \, r_{\rm vir}$, just prior to cooling onto the centrally forming galaxy. Both of these two cases – gradual heating and persistent low entropy – are sub-dominant, accounting geometrically for only $\sim 15\%$ of the total 4π, with a strong shock covering the other $\sim 85\%$.

• Finally, we conclude by assessing the ashpericity of halo gas and by measuring the location and width of the virial-

ization boundary as demarcated by temperature. We find that the distributions of maximum radius r_{max}, where the temperature exceeds e.g. $(0.1 - 0.5) \times T_{vir}$ along each radial sightline, can be quite broad. In general, for the less disturbed systems, the majority of radial sightlines first exceed $0.5\,T_{vir}$ at a well-defined surface sitting at or just beyond r_{vir}. However, a non-negligible number already exceed this temperature at larger distance, and an even larger fraction cross this threshold only inside the virial radius, between $0.5 - 0.75\,r_{vir}$. We propose that this geometrically-motivated analysis can be used to quantify the structure of gas heating as a result of the halo-IGM transition.

In order to serve as a benchmark for the realization of these eight haloes, we have intentionally not included existing models for energetic feedback due to star formation (in the form of a kinetic galactic-scale wind generation) and AGN (in the form of quasar and radio mode thermal energy input plus local radiative effects). We have deferred any direct comparisons with observations of the gas content of haloes. Both points remain directions for future work, particularly in the sense of how simulations *without* galactic winds can reproduce observed hydrogen and metal signatures. The answer may depend sensitively on details of the numerics, including hydrodynamic resolution, particularly if the spatial scale of dense gas structures in galactic haloes is as small as commonly estimated.

REFERENCES

Abadi M. G., Navarro J. F., Steinmetz M., Eke V. R., 2003, ApJ, 591, 499

Agertz O., Teyssier R., Moore B., 2009, MNRAS, 397, L64

Aragon-Calvo M. A., Neyrinck M. C., Silk J., 2014, ArXiv e-prints,

Barkana R., Loeb A., 2001, Physics Reports, 349, 125

Barnes J., Efstathiou G., 1987, ApJ, 319, 575

Barnes J., Hut P., 1986, Nature, 324, 446

Bird S., Vogelsberger M., Haehnelt M., Sijacki D., Genel S., Torrey P., Springel V., Hernquist L., 2014, MNRAS, 445, 2313

Birnboim Y., Dekel A., 2003a, MNRAS, 345, 349

Birnboim Y., Dekel A., 2003b, MNRAS, 345, 349

Birnboim Y., Dekel A., Neistein E., 2007, MNRAS, 380, 339

Bullock J. S., Dekel A., Kolatt T. S., Kravtsov A. V., Klypin A. A., Porciani C., Primack J. R., 2001, ApJ, 555, 240

Churchill C. W., Vander Vliet J. R., Trujillo-Gomez S., Kacprzak G. G., Klypin A., 2014, ArXiv e-prints,

Crighton N. H. M., Hennawi J. F., Simcoe R. A., Cooksey K. L., Murphy M. T., Fumagalli M., Prochaska J. X., Shanks T., 2015, MNRAS, 446, 18

Danovich M., Dekel A., Hahn O., Teyssier R., 2012, MNRAS, 422, 1732

Danovich M., Dekel A., Hahn O., Ceverino D., Primack J., 2014, preprint, (arXiv:1407.7129),

Dekel A., et al., 2009, Nature, 457, 451

Dolag K., Borgani S., Murante G., Springel V., 2009, MNRAS, 399, 497

Dubois Y., et al., 2014, MNRAS, 444, 1453

Faucher-Giguère C.-A., Lidz A., Zaldarriaga M., Hernquist L., 2009, ApJ, 703, 1416

Faucher-Giguère C.-A., Kereš D., Ma C.-P., 2011, MNRAS, 417, 2982

Faucher-Giguere C.-A., Hopkins P. F., Keres D., Muratov A. L., Quataert E., Murray N., 2014, ArXiv e-prints,

Feldmann R., Mayer L., 2015, MNRAS, 446, 1939

Ford A. B., Oppenheimer B. D., Davé R., Katz N., Kollmeier J. A., Weinberg D. H., 2013, MNRAS, 432, 89

Ford A. B., Davé R., Oppenheimer B. D., Katz N., Kollmeier J. A., Thompson R., Weinberg D. H., 2014, MNRAS, 444, 1260

Fumagalli M., Hennawi J. F., Prochaska J. X., Kasen D., Dekel A., Ceverino D., Primack J., 2014, ApJ, 780, 74

Gabor J. M., Bournaud F., 2014, MNRAS, 437, L56

Gabor J. M., Davé R., 2012, MNRAS, 427, 1816

Genel S., Vogelsberger M., Nelson D., Sijacki D., Springel V., Hernquist L., 2013, MNRAS, 435, 1426

George M. R., Fabian A. C., Sanders J. S., Young A. J., Russell H. R., 2009, MNRAS, 395, 657

Górski K. M., Hivon E., Banday A. J., Wandelt B. D., Hansen F. K., Reinecke M., Bartelmann M., 2005, ApJ, 622, 759

Hahn O., Abel T., 2011, MNRAS, 415, 2101

Hahn O., Angulo R., 2015, preprint, (arXiv:1501.01959),

Hennawi J. F., et al., 2006, ApJ, 651, 61

Hummels C. B., Bryan G. L., Smith B. D., Turk M. J., 2013, MNRAS, 430, 1548

Iapichino L., Adamek J., Schmidt W., Niemeyer J. C., 2008, MNRAS, 388, 1079

Joung M. R., Putman M. E., Bryan G. L., Fernández X., Peek J. E. G., 2012, ApJ, 759, 137

Katz N., Weinberg D. H., Hernquist L., 1996, ApJS, 105, 19

Katz N., Keres D., Dave R., Weinberg D. H., 2003, in Rosenberg J. L., Putman M. E., eds, Astrophysics and Space Science Library Vol. 281, The IGM/Galaxy Connection. The Distribution of Baryons at z=0. p. 185, `arXiv:astro-ph/0209279`

Kereš D., Katz N., Weinberg D. H., Davé R., 2005, MNRAS, 363, 2

Kereš D., Katz N., Fardal M., Davé R., Weinberg D. H., 2009, MNRAS, 395, 160

Khandai N., Di Matteo T., Croft R., Wilkins S. M., Feng

Y., Tucker E., DeGraf C., Liu M.-S., 2014, preprint, (arXiv:1402.0888),

Lewis A., Challinor A., Lasenby A., 2000, ApJ, 538, 473

Makino N., Sasaki S., Suto Y., 1998, ApJ, 497, 555

Marinacci F., Pakmor R., Springel V., 2014a, MNRAS, 437, 1750

Marinacci F., Pakmor R., Springel V., Simpson C. M., 2014b, MNRAS, 442, 3745

Miniati F., 2014, ApJ, 782, 21

Muratov A. L., Keres D., Faucher-Giguere C.-A., Hopkins P. F., Quataert E., Murray N., 2015, ArXiv e-prints,

Nelson D., Vogelsberger M., Genel S., Sijacki D., Kereš D., Springel V., Hernquist L., 2013, MNRAS, 429, 3353

Nelson D., Genel S., Vogelsberger M., Springel V., Sijacki D., Torrey P., Hernquist L., 2015, MNRAS, 448, 59

Oñorbe J., Garrison-Kimmel S., Maller A. H., Bullock J. S., Rocha M., Hahn O., 2014, MNRAS, 437, 1894

Ocvirk P., Pichon C., Teyssier R., 2008, MNRAS, 390, 1326

Oppenheimer B. D., Davé R., Kereš D., Fardal M., Katz N., Kollmeier J. A., Weinberg D. H., 2010, MNRAS, 406, 2325

Petitjean P., Aracil B., Srianand R., Ibata R., 2000, A&A, 359, 457

Pieri M. M., et al., 2014, MNRAS, 441, 1718

Prochaska J. X., Hennawi J. F., Simcoe R. A., 2013, ApJL, 762, L19

Prochaska J. X., Lau M. W., Hennawi J. F., 2014, ApJ, 796, 140

Putman M. E., Peek J. E. G., Joung M. R., 2012, ARA&A, 50, 491

Rauch M., Sargent W. L. W., Barlow T. A., Carswell R. F., 2001, ApJ, 562, 76

Rees M. J., Ostriker J. P., 1977, MNRAS, 179, 541

Rodriguez-Gomez V., et al., 2015, ArXiv e-prints,

Rosdahl J., Blaizot J., 2012, MNRAS, 423, 344

Rubin K. H. R., Hennawi J. F., Prochaska J. X., Simcoe R. A., Myers A., Wingyee Lau M., 2014, ArXiv e-prints,

Rudie G. C., et al., 2012, ApJ, 750, 67

Rudie G. C., Steidel C. C., Shapley A. E., Pettini M., 2013, ApJ, 769, 146

Sánchez Almeida J., Elmegreen B. G., Muñoz-Tuñón C., Elmegreen D. M., 2014, A&ARv, 22, 71

Scannapieco C., et al., 2012, MNRAS, 423, 1726

Schaal K., Springel V., 2015, MNRAS, 446, 3992

Schaye J., Carswell R. F., Kim T.-S., 2007, MNRAS, 379, 1169

Schaye J., et al., 2015, MNRAS, 446, 521

Shen S., Madau P., Guedes J., Mayer L., Prochaska J. X., Wadsley J., 2013, ApJ, 765, 89

Silk J., 1977, ApJ, 211, 638

Simcoe R. A., Sargent W. L. W., Rauch M., Becker G., 2006, ApJ, 637, 648

Springel V., 2005, MNRAS, 364, 1105

Springel V., 2010, MNRAS, 401, 791

Springel V., Hernquist L., 2003, MNRAS, 339, 289

Springel V., White S. D. M., Tormen G., Kauffmann G., 2001, MNRAS, 328, 726

Steidel C. C., Erb D. K., Shapley A. E., Pettini M., Reddy N., Bogosavljević M., Rudie G. C., Rakic O., 2010, ApJ, 717, 289

Suresh J., Bird S., Vogelsberger M., Genel S., Torrey P., Sijacki D., Springel V., Hernquist L., 2015, preprint,

(arXiv:1501.02267),

Suto Y., Sasaki S., Makino N., 1998, ApJ, 509, 544

Turner M. L., Schaye J., Steidel C. C., Rudie G. C., Strom A. L., 2014a, ArXiv e-prints,

Turner M. L., Schaye J., Steidel C. C., Rudie G. C., Strom A. L., 2014b, MNRAS, 445, 794

Vogelsberger M., Sijacki D., Kereš D., Springel V., Hernquist L., 2012, MNRAS, 425, 3024

Vogelsberger M., et al., 2014, Nature, 509, 177

Wetzel A. R., Nagai D., 2014, ArXiv e-prints,

White S. D. M., Frenk C. S., 1991, ApJ, 379, 52

White S. D. M., Rees M. J., 1978, MNRAS, 183, 341

Yoshikawa K., Yoshida N., Umemura M., 2013, ApJ, 762, 116

Zavala J., Balogh M. L., Afshordi N., Ro S., 2012, MNRAS, 426, 3464

van Leer B., 1977, J. Comput. Phys., 23, 276

van de Voort F., Schaye J., 2012, MNRAS, p. 2882